Solar wind driving of dayside field-aligned currents

Simon Wing,[1] Shin-ichi Ohtani,[1] Jay R. Johnson,[2] Marius Echim,[3,4] Patrick T. Newell,[1] Tomoyuki Higuchi,[5] Genta Ueno,[5] and Gordon R. Wilson[6]

Received 17 February 2011; revised 30 March 2011; accepted 25 April 2011; published 4 August 2011.

[1] Variations in the dayside field-aligned current (FAC) density ($J_{//}$), field-aligned parallel potential drop ($\Delta\phi_{//}$), peak precipitating electron energy (peak E_e), and precipitating electron energy flux (ε) as functions of solar wind (SW) and interplanetary magnetic field (IMF) are investigated with Defense Meteorological Satellite Program observations and a quasi-stationary low-latitude boundary layer (LLBL)–FAC coupling model. Region 1 (R1) $J_{//}$ responses to variations in SW velocity (V_{sw}) and density (n_{sw}) at 8–16 magnetic local time (MLT) suggest that R1 at these local times is frequently open while R1 at 6–08 and 17–18 MLT is frequently closed. R2 is located mostly on closed field lines. In the afternoon open R1 at 12–16 MLT, an increase in n_{sw} increases $J_{//}$, decreases maximum peak E_e (proxy for $\Delta\phi_{//}$), but has little effect on maximum ε. In the same R1 region, an increase in V_{sw} increases $J_{//}$, maximum peak E_e, and maximum ε. The dependencies of $J_{//}$, maximum peak E_e, and maximum ε are consistent with the Knight relation and the voltage generator at the magnetopause boundary in the afternoon open R1. In the midmorning and midafternoon, the response of $J_{//}$ to V_{sw} is higher for southward than for northward IMF. This can be attributed to the higher-velocity shear at the magnetopause boundary due to higher sunward convection in the LLBL inside the magnetopause. R1 in the closed-field lines near dawn and dusk appears to be more sensitive to merging rate ($d\Phi/dt = V_{sw}^{4/3} B_T^{2/3} \sin^{8/3}(\theta_c/2)$) than to SW dynamic pressure.

Citation: Wing, S., S. Ohtani, J. R. Johnson, M. Echim, P. T. Newell, T. Higuchi, G. Ueno, and G. R. Wilson (2011), Solar wind driving of dayside field-aligned currents, *J. Geophys. Res.*, *116*, A08208, doi:10.1029/2011JA016579.

1. Introduction

[2] It has been long recognized that solar wind (SW) is the primary driver of the Earth's magnetosphere [e.g., *Dungey*, 1961; *Axford and Hines*, 1974]. In the polar region, many studies show that the auroral oval size, location, and particle precipitation have dependences on SW and interplanetary magnetic field (IMF) [e.g., *Newell and Meng*, 1994; *Newell et al.*, 2004; *Wing et al.*, 1996, 2001]. The dependence of field-aligned current (FAC) pattern and density ($J_{//}$) on IMF have been well studied [e.g., *Iijima and Potemra*, 1982; *Anderson et al.*, 2008; *Papitashvili et al.*, 2002; *Weimer*, 2001; *Rostoker et al.*, 1982; *Taguchi et al.*, 1993; *Vennerstrom et al.*, 2005]. There have been relatively fewer studies of FAC dependence on SW dynamic pressure [*Keller et al.*, 2002; *Nakano et al.*, 2009; *Iijima and Potemra*, 1982]. There are even fewer studies on the FAC dependences on SW velocity (V_{sw}) and density (n_{sw}). In particular, the $J_{//}$ local time dependences on V_{sw}, n_{sw}, SW dynamic pressure, and merging rate have not been systematically investigated.

[3] It may be expected that the effect of V_{sw} and n_{sw} on FACs would be different for open and closed field lines. In the open region, the velocity shear acts as a voltage source on open field lines [e.g., *Sonnerup*, 1980; *Stern*, 1983; *Siscoe et al.*, 1991]. This process has been recently modeled by *Echim et al.* [2007, 2008]. On the other hand, in the closed field lines, plasma pressure gradient can play an important role in FAC generation [e.g., *Zaharia and Cheng*, 2003; *Wing and Newell*, 2000].

[4] Recently, *Wing et al.* [2010] statistically determines the source regions of the FACs by using simultaneously observed low-altitude particle precipitation and magnetic field measurements obtained from Defense Meteorological Satellite Program (DMSP) satellites 1983–2006. The study uses the *Higuchi and Ohtani* [2000] algorithm to automatically identify the presence of large-scale FAC current sheets using DMSP magnetometer data. To identify the FAC source regions, the study uses an automated algorithm that identifies precipitating particle source regions in the DMSP particle data and that has been developed over a time span of almost a decade [*Newell and Meng*, 1988; *Newell et al.*, 1991a, 1991b, 1991c]. The *Wing et al.*

[1]Johns Hopkins University Applied Physics Laboratory, Laurel, Maryland, USA.
[2]Plasma Physics Laboratory, Princeton University, Princeton, New Jersey, USA.
[3]Institut d'Aeronomie Spatiale de Belgique, Brussels, Belgium.
[4]Institute for Space Sciences, Bucharest, Romania.
[5]Department of Statistical Modeling, Institute of Statistical Mathematics, Tokyo, Japan.
[6]Air Force Research Laboratory, Albuquerque, New Mexico, USA.

0148-0227/11/2011JA016579

[2010] study helps illuminate when, where, and how frequently region 2 (R2), region 1 (R1), and region 0 (R0) are located on open or closed field lines. The present study examines R1 and R2 dependencies on SW and IMF with particular emphases on how these dependencies differ on open and closed field lines and on local times.

2. Knight and Current-Voltage Relationships in the Open Upward Field-Aligned Current Region

[5] FACs can be located on open and closed field lines. Here, we would like to explore how n_{sw} and V_{sw} affect the upward FAC located at the boundary layer or open field line region, for example, open afternoon R1 region. According to the linearized Knight relation [*Knight*, 1973; *Lyons et al.*, 1979; *Lyons*, 1981], in the upward FAC region, the current due to the precipitating electrons is given by

$$J_{//} = K\Delta\phi_{//} \tag{1}$$

and

$$K = \frac{n_e e^2}{(2\pi m_e k_b T_e)^{0.5}}, \tag{2}$$

where $\Delta\phi_{//}$ is field-aligned potential drop, which equals $\phi_i - \phi_m$; ϕ_i is ionospheric potential; ϕ_m is magnetospheric potential; n_e is electron number density; e is electron charge; m_e is electron mass; k_b is Boltzman constant; and T_e is electron temperature. These electron parameters refer to the electrons at the source regions in the magnetosphere.

[6] In order to gain some simple understanding of the Knight relation and current-voltage relation in the upward field-aligned current that is located at the boundary layer and/or open-field line, we consider the *Echim et al.* [2007, 2008] model equations (summarized in section 9):

$$\nabla \cdot \Sigma_p \nabla\phi_i = J_{//}(\phi_m, \phi_i) \tag{3}$$

where Σ_p = height-integrated Pedersen conductivity; ϕ_m profile is determined primarily by V_{sw}, for example, velocity shear at the boundary layer; and $J_{//}$ is determined by a current-voltage relationship in equation (1), which we assume herein to be linear. With these equations and assuming constant conductivity, it can be obtained that

$$\frac{\Sigma_p}{K}\nabla^2\phi_i = (\phi_i - \phi_m). \tag{4}$$

Taking the Fourier transform,

$$J_{//} = \sum\nolimits_q J_{//q} e^{iqx}, \tag{5}$$

we find that

$$\phi_{iq} = \left(\frac{1}{1 + \frac{\Sigma_p q^2}{K}}\right)\phi_{mq}, \tag{6}$$

$$\Delta\phi_q = \phi_{iq} - \phi_{mq} = -\left(\frac{1}{1 + \frac{K}{\Sigma_p q^2}}\right)\phi_{mq}, \tag{7}$$

and

$$J_{//q} = -\left(\frac{\Sigma_p q^2}{1 + \frac{\Sigma_p q^2}{K}}\right)\phi_{mq}. \tag{8}$$

From these expressions, it can be seen that the Fourier coefficients of $\Delta\phi$ are reduced when n_{sw} is increased, while the coefficients of $J_{//}$ are increased with increasing n_{sw}. This dependence should lead to larger $J_{//}$, but smaller $\Delta\phi$ as the solar wind n increases.

[7] As an example, consider a velocity profile across the magnetopause that has the profile $V_y(x) = (V_o/2)\,(1 + \tanh(x/\Delta))$, which is supported by a potential of the form

$$\phi_m = \frac{V_o B_o}{2}\left[x + \Delta\log\left(2\cosh\left(\frac{x}{\Delta}\right)\right)\right], \tag{9}$$

where Δ is thickness of the boundary layer, V_o is magnetosheath V, B_o is magnetosheath B, and x is the position in the direction perpendicular to the magnetopause. We have added an arbitrary constant so that the potential is zero at the magnetospheric edge of the boundary layer. Equation (9) suggests that in this simple treatment, an increase in solar wind/magnetosheath V would lead to an increase in magnetospheric potential, ϕ_m, which, in turn, leads to an increase in $J_{//}$ as suggested in equation (8). We explore $J_{//}$ and particle precipitation dependence on the solar wind/magnetosheath V and n observationally in sections 7 and 8 and with the *Echim et al.* [2007, 2008] model in section 9.

3. Data and Method

[8] The present study used data from the particle (SSJ4) and magnetic field instruments onboard DMSP satellites. DMSP satellites are Sun-synchronous satellites in nearly circular polar orbit at an altitude of roughly 835 km and with a period of approximately 101 min per orbit.

[9] The SSJ4 instrument package included on all recent DMSP flights uses curved plate electrostatic analyzers to measure ions and electrons from 32 eV to 30 keV in logarithmically spaced steps [*Hardy et al.*, 1984]. Because of its upward pointing and limited pitch angle resolution, DMSP SSJ4 measures only highly field-aligned precipitating particles.

[10] The DMSP magnetic field experiments consist of triaxial fluxgate magnetometers with a range of ±65535 nT and one-bit resolution of 2 nT [*Rich et al.*, 1985]. The time resolution is 1 s.

[11] In the present study, we used over 20 years of simultaneous DMSP magnetic field and particle precipitation (SSJ4) observations, 1983–2006, to determine the source regions of R2 and R1. However, not all DMSP satellites carry a magnetometer, although all carry the SSJ4 instrument during this period. Because we are interested only in the periods when there is simultaneous magnetic field and particle precipitation data, our data set is limited to the periods when both data sets are present. These periods are DMSP-F7 (December 1983 to January 1988), and F12 (September 1994 to July 2002), F13 (March 1995 to November 2006), F14 (April 1997 to November 2006), F15

(December 1999 to November 2006), and F16 (December 2003 to November 2006).

[12] Solar wind data were obtained from ACE, WIND, IMP8, ISEE1, and ISEE3 observations. The ACE SWEPAM and MAG data; and the WIND MAG data were obtained from CDAWeb. The WIND 3DP data were obtained from the 3DP team directly. The ISEE1 and ISEE3 data were obtained from UCLA. The IMP8 data came directly from the IMP teams. The solar wind was propagated with minimum variance technique [*Weimer et al.*, 2003] to GSM $(X, Y, Z) = (17, 0, 0)\ R_E$ to produce 1 min files. For simplicity, a 10 min propagation time was estimated from $(X, Y, Z) = (17, 0, 0)\ R_E$ to the ionosphere (~2 min propagation time from $X = 17\ R_E$ to nominal magnetopause location at $X = 10\ R_E$ with $V_{sw} = 450$ km s^{-1}; 5–6 min is added for the delay in magnetosheath [e.g., *Lockwood et al.*, 1989, *Spreiter and Stahara*, 1985]; ~2–3 min Alfvén wave propagation from the magnetopause to the ionosphere [*Keller et al.*, 2002; *Lockwood et al.*, 1989; *Rostoker et al.*, 1982]. The exact propagation time is not crucial because only the 30 min averages were calculated and used. The 30 min averages were centered on the time of the DMSP encounter with the equatormost boundary of FAC. These 30 min averages of SW and IMF parameters were assigned for the entire FAC encounter. Because DMSP crosses FAC or the auroral oval four times per orbit, four 30 min SW and IMF averages were calculated per orbit per spacecraft.

4. Method for Obtaining Field-Aligned Currents

[13] For this study, we applied the automated algorithm that identifies the large-scale structure of FACs developed by *Higuchi and Ohtani* [2000] on DMSP magnetic field data. Two of the magnetic field components lie on the horizontal plane, the plane parallel to the surface of the Earth. From these two components, the minimum and maximum variances of the magnetic field are obtained and denoted by B_L and B_A, respectively. B_L is approximately in the latitudinal direction, typically the direction of the satellite trajectory, whereas B_A in the azimuthal direction, approximately parallel to the FAC sheets. Thus, if FACs have large sheet structures, then the magnetic field variation should be confined primarily to B_A only. B_A increases or decreases as the satellite orbits the Earth. The *Higuchi and Ohtani* [2000] algorithm uses the first-order B spline to fit line segments to B_A variations from the pole to approximately about 40° magnetic latitude (MLAT). If the distribution of large-scale (>1°) FAC can be approximated as an infinite sheet, each line segment corresponds to the crossing of a FAC sheet. This algorithm is essentially the automation of the way we visually examine a plot of satellite magnetic field data. Auroral crossings with data gaps are not processed. A more detailed description of the algorithm is provided by *Higuchi and Ohtani* [2000].

5. Dayside FAC Source Regions

[14] Magnetospheric particles move along the magnetic field lines and a fraction precipitate in the ionosphere. The differences in the source regions and structures along the field line lead to the different signatures of the precipitating particles. *Newell and Meng* [1988] and *Newell et al.* [1991a, 1991b, 1991c] developed an automated algorithm to determine the particle precipitation region that provides information about the origins of these precipitating particles in the magnetosphere or solar wind. For the present study, an important piece of information that these particle signatures can give is whether or not these particles are located on open or closed field lines.

[15] The particle precipitation identification algorithm classifies the dayside polar region into nine regions: radiation belt (rad), central plasma sheet (CPS), boundary plasma sheet (BPS), open-field line low-latitude boundary layer (open-LLBL), cusp, mantle, polar rain, and void. The morphology and interpretation of the origins of these particles have been given by *Newell and Meng* [1988], *Newell et al.* [1991a, 1991b, 1991c], and *Wing et al.* [2010, and references therein]. For the present study, it is sufficient to note that rad, CPS, BPS, and void particles are located on closed field lines whereas open-LLBL, cusp, mantle, and polar rain are located on open field lines. The low-latitude boundary layer (LLBL) contains mixtures of magnetosheath like cold plasma and magnetospheric proper hot plasma that is commonly found near the magnetopause boundary. As such, it can be open or closed. BPS* is the region that is classified as BPS by the particle precipitation region identification algorithm [*Newell and Meng*, 1988; *Newell et al.*, 1991a, 1991b, 1991c], but some of the BPS particles really correspond to the mantle particles that have gone through the upward field-aligned electric field that sometimes exists within some upward R0 and R1 regions. Hence, unlike BPS, which is closed, BPS* may be open or closed (see *Wing et al.* [2010] for the full description). Void, which is usually found equatorward of CPS, most likely corresponds to inner magnetospheric region where the particles are anisotropic and more energetic. As an aside, in the open region, the algorithm can sometimes identify very weak polar rain as void, but the present study and the *Wing et al.* [2010] study have properly labeled this type of void as polar rain.

[16] *Wing et al.* [2010] applied the *Higuchi and Ohtani* [2000] and particle identification algorithm to simultaneously observed DMSP SSJ4 and magnetometer data to determine the source FAC source regions. FAC patterns can consist of two or more sheets, but two- and three-sheet patterns are the most common [e.g., *Ohtani and Higuchi*, 2000; *Wing et al.*, 2010]. The source regions for two-FAC-sheet structure is displayed in Figure 1. In Figure 1 and the present study, the data from the northern and southern hemispheres have been combined. Thus, Figure 1 can be readily compared with particle precipitation maps [*Newell and Meng*, 1992; *Newell et al.*, 2004] and FAC patterns [e.g., *Anderson et al.*, 2008; *Weimer*, 2001], which were constructed with data from both hemispheres. We have looked at the maps constructed from northern and southern hemispheres alone and found no discernible differences between the two hemispheres.

[17] Figure 1 shows that the two-FAC-sheet pattern is not symmetrical around noon. Figure 1 shows that the morning R1 and R2 patterns extend from 6 to 10 magnetic local time (MLT) while the afternoon R1 and R2 patterns extend from 11 to 18 MLT. It is interesting to note that the shift of the afternoon pattern toward prenoon (11 MLT) is consistent with the asymmetry in the averaged convection pattern that

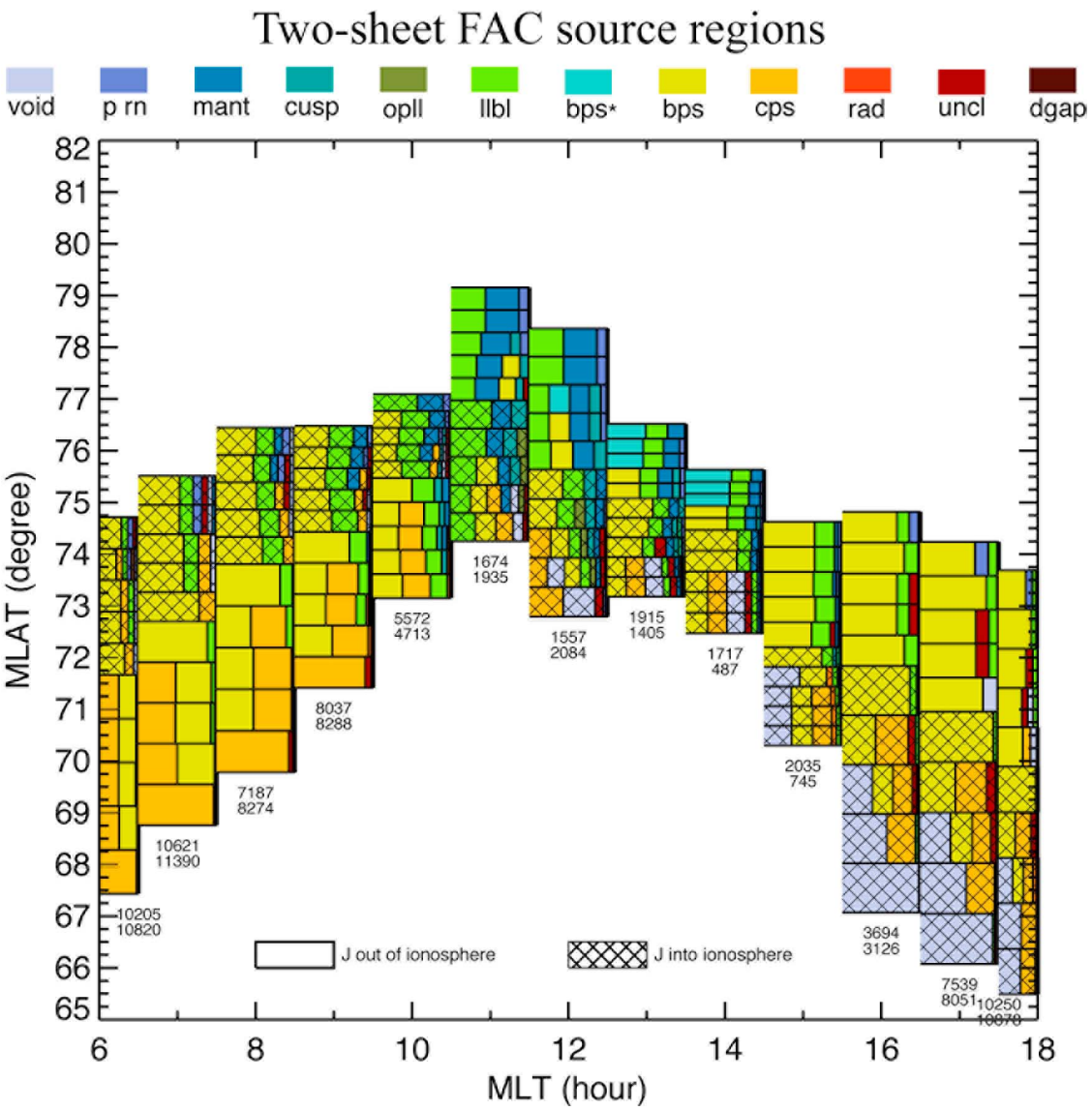

Figure 1. Source regions of two FAC sheets. The source regions are color coded using the scheme depicted in the boxes at the top. The nomenclatures used are p rn, polar rain; mant, mantle; opll, open-LLBL; uncl, unclassified; rad, radiation belt; and dgap, data gap. The particle precipitation regions are described in section 5. The hatched and nonhatched regions indicate currents flowing into and out of the ionosphere, respectively. In each MLT, each current sheet is divided into five equally spaced latitudinal regions, and within each region, the area of the source (color) region is proportional to the frequency of occurrence. The source regions are sorted from left to right in the order of descending frequency of occurrence. The numbers below R2 indicate the number of events in each current sheet: the top and bottom numbers indicate the number of events in R1 and R2, respectively. (Adapted from *Wing et al.* [2010].)

has the afternoon cell shifted to 11 MLT [e.g., *Ruohoniemi and Greenwald*, 1996; *Weimer*, 1995; *Papitashvili et al.*, 1994]. Note that the display format used in Figure 1 is different from that used by *Newell and Meng* [1992] and *Newell et al.* [2004]. *Newell and Meng* [1992] and *Newell et al.* [2004] only give the most probable particle precipitation source region for a given point in the ionosphere. In contrast, as described in the caption, Figure 1 gives all of the source regions and the probabilities of observing the particles that originate from each region. Thus, Figure 1 gives more information than *Newell and Meng* [1992] and *Newell et al.* [2004] particle precipitation maps.

[18] Figure 1 shows that R2 originates mostly from CPS and BPS in the morning and from void, BPS, and CPS in the afternoon. Hence, R2 is located mostly on closed field lines, although a tiny fraction of R2 originates from LLBL, which

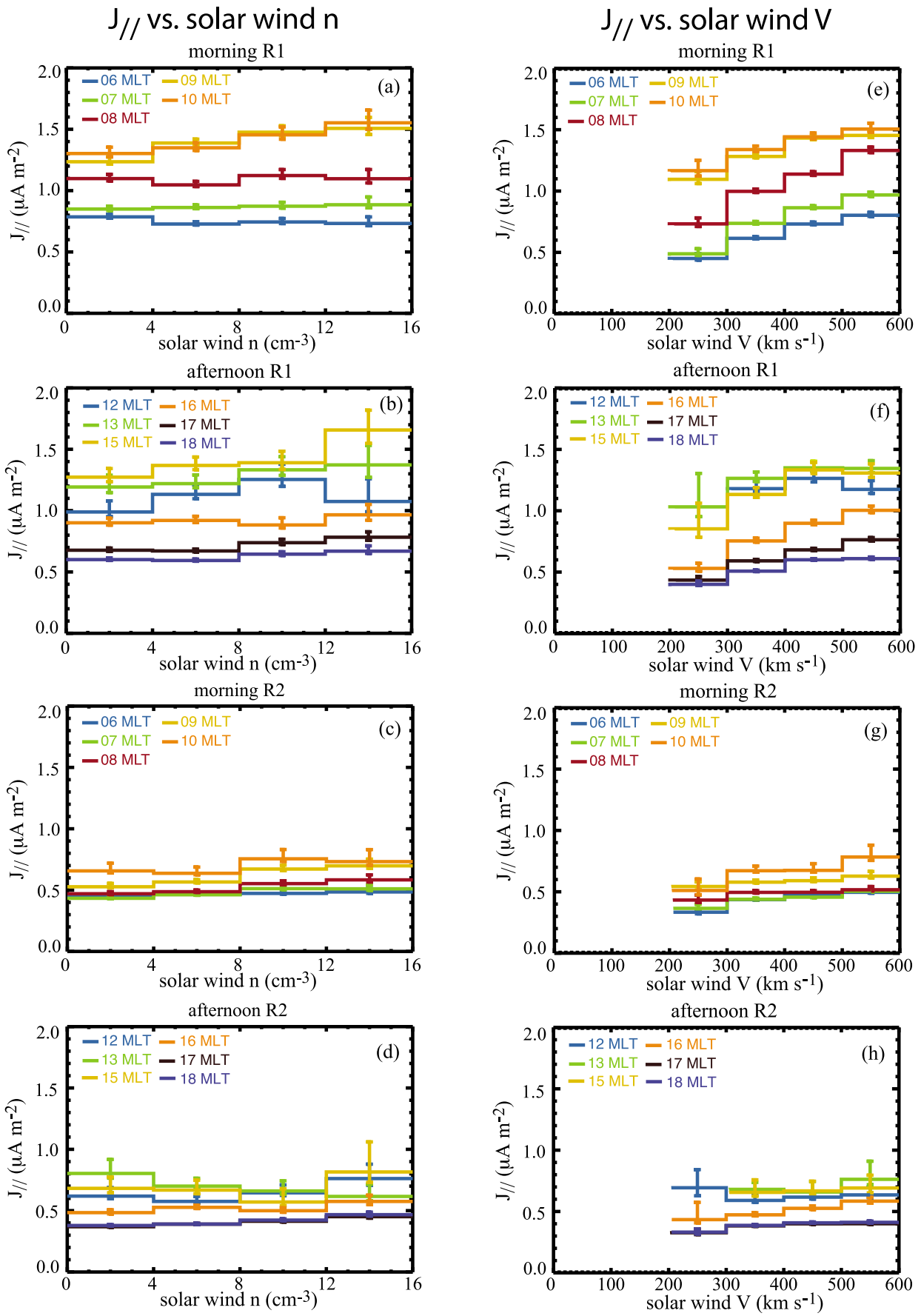
J// vs. solar wind n
J// vs. solar wind V
morning R1
afternoon R1
morning R2
afternoon R2
06 MLT
07 MLT
08 MLT
09 MLT
10 MLT
12 MLT
13 MLT
15 MLT
16 MLT
17 MLT
18 MLT
(a)
(b)
(c)
(d)
(e)
(f)
(g)
(h)
J// (μA m-2)
solar wind n (cm-3)
solar wind V (km s-1)

Figure 2

can be open or closed and located near the magnetopause. Near noon or prenoon, 10–13 MLT, LLBL becomes a more frequent source region for R2, suggesting that R2 may be more open. At these local times, R2 is located at higher latitudes than at other local times such that it has a better access to LLBL.

[19] As can be seen from Figure 1, R1 can originate from open as well as closed field lines, but the relative composition or occurrence rate varies with MLT and latitude. In the morning and afternoon, R1 mostly originates from BPS, which is closed, and a much smaller fraction originates from LLBL, which may be open or closed and located near the magnetopause. The frequency of encountering LLBL in R1 increases toward noon. In fact, near noon, LLBL is the most dominant source region.

6. Solar Wind *n* and *V* Driving of $J_{//}$

[20] Figure 1 shows the two-current-sheet FAC source regions as a function of MLT. In order to see how n_{sw} affects $J_{//}$ in each MLT within each current sheet, we created twelve 1 h bins, centered on the hour from 6 to 18 MLT. Then, for each bin, we computed the median $J_{//}$ for each 4 cm^{-3} bin for the n_{sw} ranging from 0 to 16 cm^{-3}. The resulting $J_{//}$ versus n_{sw} are plotted in Figures 2a–2d for morning R1, afternoon R1, morning R2, and afternoon R2, respectively. These patterns correspond to those seen in Figure 1. Figures 2a and 2b show that n_{sw} does not affect morning and afternoon R1 $J_{//}$. However, around noon (9–15 MLT), R1 $J_{//}$ generally increases with n_{sw}. Figures 2c and 2d show that n_{sw} has little effect on R2 $J_{//}$. Figure 2 leaves out R1 and R2 curves for 11 and 14 MLT because they would obscure the already busy plots in Figures 2b and 2d, respectively, without adding much more information. For the same reason, 11 and 14 MLT curves are left out in other afternoon R1 and R2 plots throughout this paper.

[21] The error bars in Figures 2, 3, 4, 7, and 8 give a measure of the standard deviation of the median, σ_{median}. Assuming a normal distribution, for a large sample, as is the case in the present study, $\sigma_{\text{median}} = 1.25\ \sigma_{\text{dist}}/\text{sqrt(N)}$, where σ_{dist} is the centroid 68% of the distribution, for example, 16th–84th percentile of the distribution, and N is the number of points in the sample and ranges from a few thousands to slightly over ten thousand, as indicated in the caption of Figure 1 [e.g., *Kenney and Keeping*, 1951; *Hodges and Lehmann*, 1967].

[22] We did the same analysis for V_{sw} from 0 to 600 km s^{-1}. The results are plotted in Figures 2e–2h for morning R1, afternoon R1, morning R2, and afternoon R2, respectively; the V_{sw} bin size is 100 km s^{-1}. Figures 2e and 2f show that morning and afternoon R1 $J_{//}$ increases with V_{sw}, the slopes of the curves are positive. The slope starts out small near noon and increases toward midmorning and midafternoon, maximizing around 8 MLT and 15–16 MLT, respectively, before decreasing toward dawn and dusk. Just as with n_{sw}, the morning and afternoon R2 have little dependence on V_{sw}.

[23] If the FACs are located on open field lines or LLBL, the source regions are the inner edge of the magnetosheath or LLBL (the regions adjacent to the magnetopause). We use n_{sw} to denote both ion n_{sw} (n_{swi}) and electron n_{sw} (n_{swe}), and V_{sw} to denote both ion V_{sw} (V_{swi}) and electron V_{sw} (V_{swe}). From the charge quasi-neutrality consideration, it is expected that $n_{sw} \sim n_{swe} \sim n_{swi}$ and $V_{sw} \sim V_{swe} \sim V_{swi}$ [e.g., *Bame et al.*, 1992]. The present study has no measurement of the magnetosheath n_e and V_e, but magnetosheath n_e and V_e positively correlate with n_{sw} and V_{sw}, respectively [e.g., *Spreiter and Stahara*, 1985; *Samsonov and Hubert*, 2004]. In the LLBL within the magnetosphere, *n* and *T* are typically intermediate between those of magnetosheath and the magnetosphere proper [e.g., *Eastman et al.*, 1976; *Hasegawa et al.*, 2003; *Wing et al.*, 2005, 2006; *Johnson and Wing*, 2009]. Thus, LLBL *n* and *T* positively correlate with n_{sw} and T_{sw}, respectively.

[24] In the open upward FAC region, an increase in the magnetosheath or LLBL *n* would increase the current carriers, which in turn, would increase $J_{//}$. This can be seen from equations (2) and (8), which suggest that an increase in *n* would increase *K* and hence $J_{//}$. Indeed, this relationship is observed in the afternoon R1 pattern near noon in Figure 2b, where the currents flow upward (out of the ionosphere) and are carried mostly by the downward precipitating electrons [e.g., *Burch et al.*, 1983]. Figure 2b shows that near noon (12–15 MLT), $J_{//}$ increases with n_{sw}, suggesting that at these local times, the field lines are mostly open. In contrast, in the late afternoon (16–18 MLT), $J_{//}$ is less sensitive to n_{sw}. There could be two possible reasons for this. First, in the late afternoon, the field lines are more frequently closed than open. Second, at these local times, the field lines map further downstream to the tail flanks. For a given Δn_{sw}, Δmagnetosheath *n* is larger at the subsolar region around noon than in the flanks. For example, in the *Spreiter and Stahara* [1985] magnetosheath model, $n = 4.2\ n_{sw}$ at noon, but $n = 1.6\ n_{sw}$ at the dusk and dawn flanks.

[25] Similar behavior is also observed in the morning R1. Figure 2a shows that near noon, 9–10 MLT, $J_{//}$ increases with n_{sw} while in the early morning, 6–8 MLT, $J_{//}$ is hardly affected by n_{sw}. However, the interpretation for the morning R1 is not as straightforward as afternoon R1 because in the morning R1, the currents flow downward, instead of upward. Hence, the source region of the electrons is not SW and n_{sw} should not directly affect $J_{//}$. Therefore, it is quite interesting to see that at 9–10 MLT, $J_{//}$ correlates positively with n_{sw}. Morning R1 $J_{//}$ may connect or close with afternoon R1 $J_{//}$, which is affected by the n_{sw} as shown in Figure 2b.

[26] Near the magnetopause boundary, an increase in the magnetosheath speed leads to an increase in the velocity shear and the voltage drop across the magnetopause boundary, which in turn, leads to larger $J_{//}$, as suggested from equations (8) and (9), assuming ionospheric conduc-

Figure 2. $J_{//}$ dependence on solar wind *n* and *V*. Median $J_{//}$ versus n_{sw} for (a) morning R1, (b) afternoon R1, (c) morning R2, and (d) afternoon R2. Median $J_{//}$ versus V_{sw} for (e) morning R1, (f) afternoon R1, (g) morning R2, and (h) afternoon R2. Median $J_{//}$ for each MLT is calculated in 4 cm^{-3} bin in Figures 2a–2d and in 100 km s^{-1} bins in Figures 2e–2h. The $J_{//}$ curve for each MLT is color coded with the scheme shown in each frame.

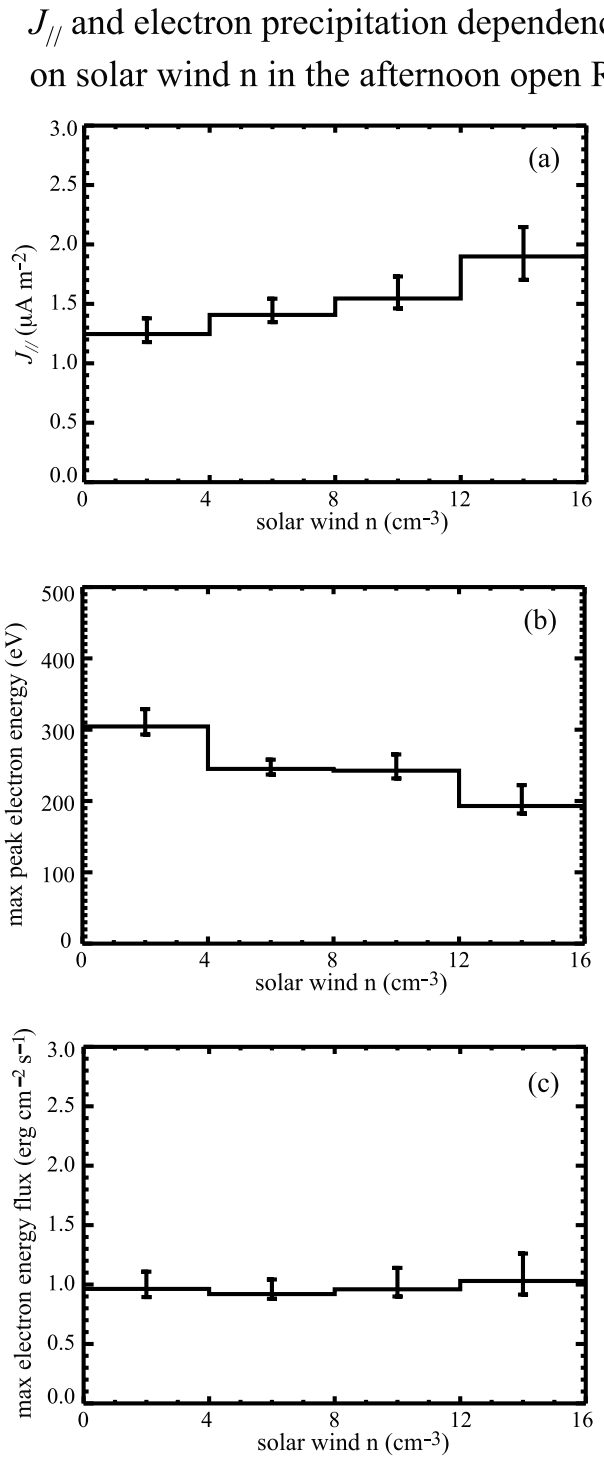

Figure 3. Open afternoon R1 $J_{//}$ and particle precipitation dependence on n_{sw}: (a) median $J_{//}$, (b) median maximum peak precipitating electron energy, and (c) median maximum precipitating electron energy flux in the afternoon R1 12–16 MLT that map to open-LLBL, LLBL, cusp, mantle, and polar rain. The median $J_{//}$ s are calculated in 4 cm^{-3} bins.

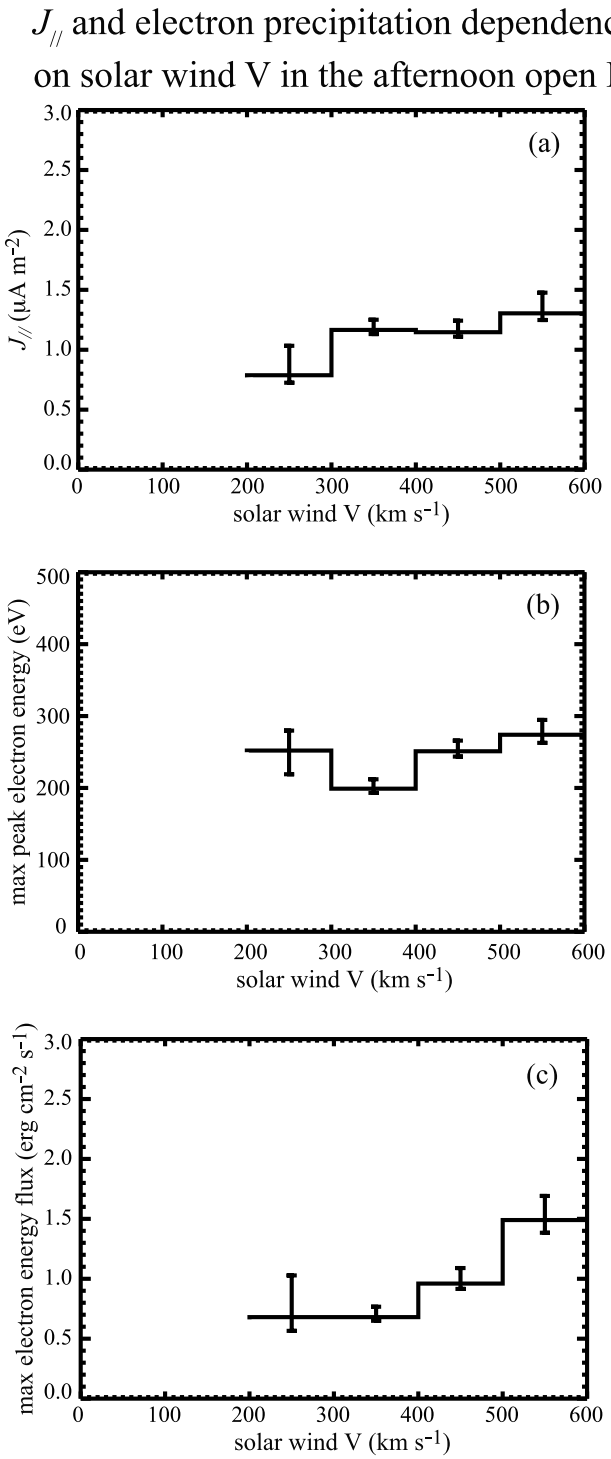

Figure 4. Open afternoon R1 $J_{//}$ and particle precipitation dependence on solar wind V: (a) median $J_{//}$, (b) median maximum peak precipitating electron energy, and (c) median maximum precipitating electron energy flux in the afternoon R1 12–16 MLT that map to open-LLBL, LLBL, cusp, mantle, and polar rain. The median $J_{//}$ values are calculated in 100 km s^{-1} bins.

tivity and other parameters remain the same. However, there is a local time dependence. The magnetosheath speed increases with the antisunward distance down the tail and higher V_{sw} leads to a larger magnetosheath V. For example, in the *Spreiter and Stahara* [1985] magnetosheath model, $V \sim 0\ V_{sw}$ at the subsolar region, but $V \sim 0.8\ V_{sw}$ at the dawn and dusk flanks. Thus, based on this magnetosheath speed profile, for a given ΔV_{sw}, $\Delta J_{//}$ should asymptotically increase from noon toward dusk and dawn. This is consistent with Figures 2e and 2f. In Figures 2e and 2f, the slope starts out small near noon and increases to a peak value in the midmorning (8 MLT) and in the midafternoon (15–16 MLT) before decreasing at dawn (6–7 MLT) and at dusk (17–18 MLT). The slope decreases at 17–18 MLT and 6–7 MLT suggest that the field lines map to the magnetopause regions that are mostly closed. Hence, $J_{//}$ at these locations is less sensitive to V_{sw}. However, there is a dawn-dusk asymmetry: it seems that R1 $J_{//}$ at 6–7 MLT has stronger dependence on V_{sw} than R1 $J_{//}$ at 17–18 MLT.

[27] Figure 2 shows that neither afternoon nor morning R2 is affected much by n_{sw} and V_{sw}, which would be consistent with this current being located more frequently on closed field lines well inside the magnetosphere. However, the closed field lines could be affected by SW dynamic pressure and/or merging rate, both of which have n and/or V terms. This is discussed in section 11 of this paper. SW particles can enter along the flanks and convect to the dayside, modifying the dayside closed field line pressure gradient and hence $J_{//}$. However, the timescale for this mass transport is about 8 h at dawn and dusk and 15 h on the dayside [e.g., *Borovsky et al.*, 1998], whereas the present study uses only 30 min averaged simultaneous SW observations. Thus, the present study investigates only the nearly simultaneous SW effects. Substorms and storms, of course, can affect FACs, particularly at dusk, but the present study does not focus on substorm and/or storm effects.

[28] Figures 1 and 2 are constructed from data that are independent of each other. Figure 1 is obtained from combining DMSP magnetic field and particle data, while Figure 2 is obtained from combining DMSP magnetic field and SW data. Yet, both Figures 1 and 2 present the same consistent picture of the open and closed nature of the R1 and R2 regions. That is, (1) R1 is mostly open near noon, but mostly closed near dawn and dusk, and (2) R2 is mostly closed.

[29] In general, there is a gradient of $J_{//}$ with MLT such that $J_{//}$ is higher closer to noon, as shown in Figure 2. This may be related to conductivity from solar EUV being higher closer noon [e.g., *Robinson and Vondrak*, 1984], although there may be other factors as well. This would be consistent with the model results discussed in section 9, which show that higher conductivity leads to higher $J_{//}$.

7. Open Afternoon R1 $J_{//}$ and Electron Precipitation Dependence on n_{sw}

[30] In section 6, at 12–16 MLT, R1 $J_{//}$ dependence on n_{sw} and V_{sw} suggests that R1 at these local times is open at least some of the time or even most of the time. It does not mean that at these local times R1 is open all the time. In fact, section 5 and *Wing et al.* [2010] describe how we statistically determined how often R1 is open through the use of simultaneously observed particle data. Using the simultaneously observed particle and magnetometer data sets, we selected the afternoon R1 when the particle signatures indicate that the entire R1 is on open-field lines or at the boundary near the magnetopause, namely the regions that correspond to LLBL, open-LLBL, cusp, mantle, and polar rain.

[31] Figure 3a shows median afternoon R1 $J_{//}$ versus n_{sw} for the open region or LLBL for 12–16 MLT in a 4 cm^{-3} n_{sw} bin size. Because R1 at 17–18 MLT is rarely open or within LLBL, it is not included. Figure 3a shows that $J_{//}$ increases with increasing n_{sw}. This is similar to Figure 2b, except that Figure 2b shows $J_{//}$ for each MLT obtained from all regions, open and closed. As a result of the more restrictive criterion for the data selection, Figure 3 contains fewer points than Figure 2b. In Figure 3, the numbers of points in the [0, 4], [4, 8], [8, 12], and [12, 16] cm^{-3} bins are 162, 302, 154, and 67, respectively.

[32] The present study has no direct measurement of the field-aligned potential drop or $\Delta\phi_{//}$. However, studies have shown that $\Delta\phi_{//}$ can be estimated reasonably well from the peak precipitating electron energy in the electron acceleration or "inverted V" region within the upward field-aligned current region [e.g., *Lyons et al.*, 1979; *Reiff et al.*, 1988]. This has been shown on the nightside, particularly in the dusk–midnight sector where $\Delta\phi_{//}$ is often very large, up to about 10 keV, a few to several times larger than the electron energy in the source region above the field-aligned potential region [e.g., *Reiff et al.*, 1988]. On the dayside, at 12–16 MLT, electron acceleration events are also found, but $\Delta\phi_{//}$ is weaker, typically on the order of a few hundred eVs to a few keVs [e.g., *Sonnerup*, 1980]. However, these energies are typically at least a few times larger than the dayside magnetosheath electron energy, depending on the magnetopause location [e.g., *Spreiter and Stahara*, 1985]. The maximum $\Delta\phi_{//}$ per auroral crossing should be even larger than the typical magnetosheath electron energy. Thus, we should be on firmer ground, if we use the maximum peak precipitating electron energy (E_e) per auroral crossing as a proxy for the maximum $\Delta\phi_{//}$. Although within each individual measurement, there is no guarantee that we will be able to obtain an electron acceleration event, within each auroral oval crossing, there are usually some instances of electron acceleration events or $\Delta\phi_{//}$. Hence, maximum $\Delta\phi_{//}$ or the maximum peak E_e per auroral crossings can be easily obtained. Figure 3b plots the median maximum peak E_e versus n_{sw}. The maximum peak E_e are organized in 4 cm^{-3} n_{sw} bins. Figure 3b shows that maximum peak E_e decreases with increasing n_{sw}.

[33] As discussed in section 2, an increase in n_{sw} would reduce the $\Delta\phi_{//}$ needed to maintain the same $J_{//}$. From equation (2), K increases with n_e or n_{sw}, but from equation (1), the fact that $J_{//}$ increases with n_{sw} suggests that the increase in K is larger than the decrease in $\Delta\phi_{//}$.

[34] Next, we examine how the maximum precipitating electron energy flux (ε) varies with n_{sw}. This relationship is shown in Figure 3c, which plots maximum ε versus n_{sw} for 12–16 MLT. It shows that maximum ε remains approximately constant with respect to n_{sw}. The precipitating electron energy flux $\varepsilon\ \alpha\ (n \times V_p \times \text{peak } E_e)$, where V_p =

precipitating electron velocity ~ V + sqrt(2 m^{-1} × peak E_e), and n and V are the density and velocity in the source region. If other parameters were held constant, n (source region) would increase with n_{sw}, but it is expected that the peak E_e would vary inversely with n_{sw}, as described above. Apparently, the changes in these two terms nearly cancel each other, and overall maximum ε does not vary much with n_{sw}, as shown in Figure 3c.

8. Open Afternoon R1 $J_{//}$ and Electron Precipitation Dependence on V_{sw}

[35] The present study also examines how open R1 $J_{//}$, maximum peak E_e, and maximum ε vary with V_{sw}. Figure 4 plots the median of these parameters as a function of V_{sw} in the same format as Figure 3. The V_{sw} bin size used to calculate these medians is 100 km s^{-1}. As the V_{sw} increases, the velocity shear at the magnetopause boundary increases, which leads to an increase in the electric potential drop across the magnetopause ($\Delta\mathbf{E} = \Delta\mathbf{V} \times \mathbf{B}$), which in turn leads to an increase in $J_{//}$, assuming other parameters remain constant. This can be seen from equations (8) and (9) and has been discussed in section 2. This relationship may be seen in Figure 4a, which plots $J_{//}$ versus V_{sw} when the entire R1 is on open-field line. The open R1 is determined using the same criteria that are used in section 7. As a result of the open-field line criteria, Figure 4 contains fewer points than Figure 2f. In Figure 4, the numbers of points in the [200, 300], [300, 400], [400, 500], and [500, 600] km s^{-1} bins are 20, 315, 301, and 136, respectively.

[36] Figure 4b shows that maximum peak E_e increases with V_{sw}. Section 2 discusses how an increase in V_{sw} would lead to increases in $J_{//}$ and $\Delta\phi_{//}$. The latter can be estimated with the maximum peak E_e. From the point of view of the closed circuit formed by the magnetosphere- ionosphere, the higher potential drop across the boundary at the magnetopause has to be balanced by the higher $\Delta\phi_{//}$ and/or cross-polar cap potential drop in the ionosphere. Initially, when V_{sw} is small, $\Delta\phi_{//}$ can be small because only small $J_{//}$ is needed to maintain a small ionospheric potential drop to balance the small potential drop across the magnetopause boundary. However, as V_{sw} increases, larger $J_{//}$ is needed presumably to increase the cross-polar cap potential in the ionosphere. As V_{sw} continues to increase, $J_{//}$ continues to increase, but at some point $\Delta\phi_{//}$ has to increase in order to draw more electrons downward to maintain the higher $J_{//}$. Therefore, if other parameters are held constants, maximum peak E_e can be expected to increase with V_{sw}. This can be seen in Figure 4b, except for the lowest V bin, 200–300 km s^{-1}. However, this lowest V bin has only 20 points and its value may be susceptible to variations in other parameters. For example, it may result from the data points in this bin having lower-than-average densities in a manner discussed in section 7, but unfortunately this is difficult to ascertain. This is because several of the data points come from the ACE SWEPAM instrument, which is less sensitive at low energies that roughly correspond to V below 300–350 km s^{-1}. Because of this reduced sensitivity, the densities are often underestimated and, in fact, are removed from the validated Level 2 data set used in the present study. However, it was determined that the calculation of the velocity moment is less sensitive to the uncertainties, and therefore the velocities are kept in the database (Ruth Skoug, private communication, 2010).

[37] Finally, in the expression $\varepsilon \alpha (n \times V_p \times \text{peak } E_e)$, V_p increases with V_{sw} and peak E_e also increases with V_{sw}. Hence, the overall effect is that maximum ε increases with V_{sw}, as can be seen in Figure 4c.

9. Comparisons Between Data and Model Results

9.1. A Quasi-Stationary Model for the Coupling Between the LLBL Sheared Flow Interface and the Afternoon Upward $J_{//}$

[38] Ad hoc convergent electric fields are considered by *Lyons* [1980, 1981] to describe the magnetospheric generator of FACs. *Roth et al.* [1996] and *De Keyser et al.* [1998] suggest that tangential discontinuities (TD) play a role of a magnetospheric generator. *Echim et al.* [2008, 2009] modeled the coupling between the TD generators formed at the inner edge of the magnetosheath and the magnetospheric LLBL, basically the regions adjacent to the magnetopause. The *Echim et al.* [2008] model uses a Vlasov (kinetic) equilibrium solution [*Roth et al.*, 1996; *Echim and Lemaire*, 2005] to describe the transition between the magnetospheric and magnetosheath plasma in the generator. One key feature of the kinetic description of the generator is the self-consistent convergent/divergent electric field perpendicular to the surface of discontinuity that depends on the shear of the magnetosheath bulk velocity and the magnetosheath T and n gradients. A brief description is given below, but a complete description of this model can be found in the work by *Echim et al.* [2007, 2008].

[39] The flux of magnetospheric particles precipitating into the auroral ionosphere from the magnetosheath/LLBL contributes to a net field-aligned current with density $J_{//}$. The auroral current–voltage relationship (ACVR) describes $J_{//}$ as a function of the field aligned potential drop, $\Delta\phi_{//} = \phi_i - \phi_m$, between the generator (characterized by the electric potential ϕ_m) and the auroral ionosphere (characterized by the electric potential ϕ_i). The ACVR has been derived for a monotonically decreasing $\Delta\phi_{//}$ with altitude, assuming adiabatic motion of particles along the flux tube connecting the generator and the load [*Knight*, 1973; *Lemaire and Scherer*, 1973; *Chiu and Schultz*, 1978; *Fridman and Lemaire*, 1980; *Pierrard*, 1996]. When the Hall currents are divergence free, the current continuity equation in the ionosphere requires that the net parallel current in the ionosphere $J_{//}$ be equal to the divergence of the horizontal height-integrated Pedersen current in the ionosphere (I_P):

$$J_{//}(\Delta\phi_{//}) = -\frac{dI_p}{dx_i} = \frac{d}{dx_i}\left(\Sigma_p \frac{d\phi_i}{dx_i}\right), \tag{10}$$

where x_i denotes the distance perpendicular to the arc at ionospheric altitude, and Σ_p is the height-integrated Pedersen conductivity. Equation (10) gives a quantitative description of the coupling between plasma and magnetic field properties at the magnetosheath/LLBL (the generator) and the plasma and field properties in the ionospheric load. It is solved for the unknown ϕ_i and the input parameters ϕ_m and Σ_p. The ionospheric feedback effect is introduced in equation (10) via the relationship between

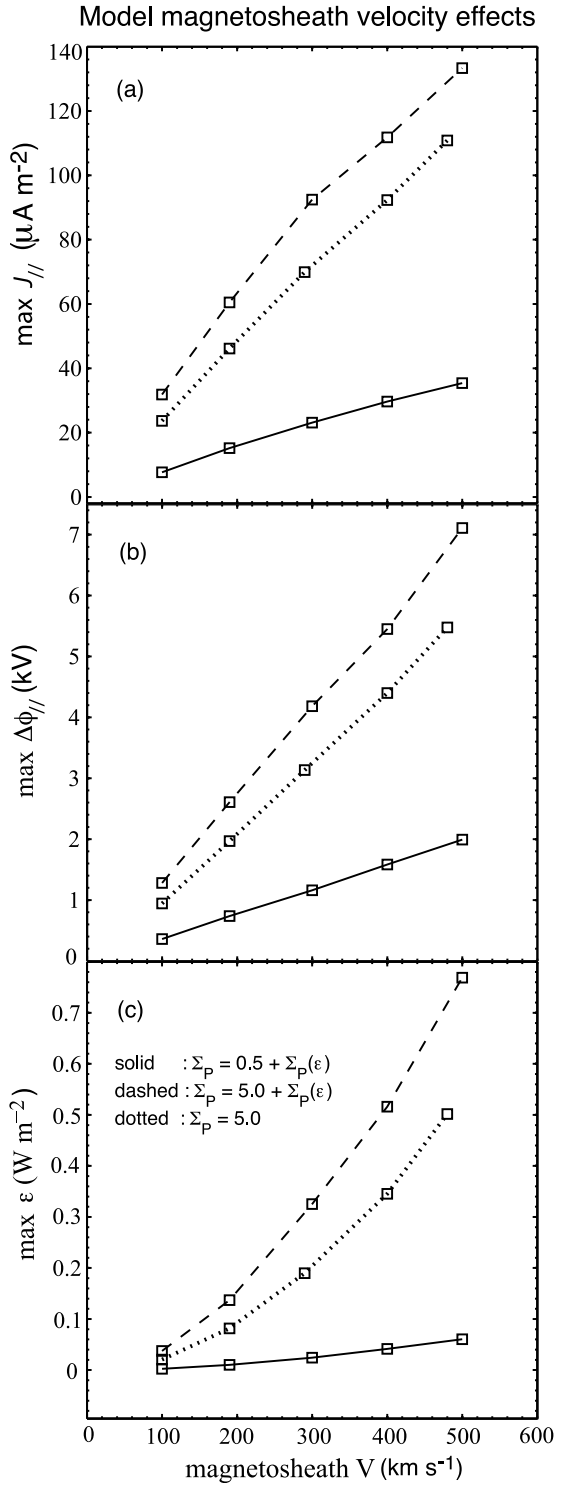

Figure 5. (a) Maximum $J_{//}$, (b) maximum $\Delta\phi_{//}$, and (c) maximum ε as a function of the bulk magnetosheath V and Σ_P. Solid lines represent results obtained for Σ_P that depends on maximum ε with a nonuniform conductance Σ_P = 0.5 S + $\Sigma_P(\varepsilon)$, dashed lines show results obtained for a nonuniform conductance with Σ_P = 5 S + $\Sigma_P(\varepsilon)$, and dotted lines correspond to results obtained for a uniform Σ_P = 5 S. (Adapted from *Echim et al.* [2008].)

Σ_P and the precipitating electron energy flux, ε [*Harel et al.*, 1977]:

$$\Sigma_p = \Sigma_{p0} + a\sqrt{\varepsilon}, \tag{11}$$

where Σ_{p0} is the base level of the ambient/background conductance produced by the solar EUV radiation. The energy flux of precipitating electrons, ε, is determined from the second-order moment of the solution of the stationary Vlasov equation [*Lemaire and Scherer*, 1973] and is a function of $\Delta\phi_{//}$:

$$\varepsilon = n_e kT_e \frac{B_i}{B_m}\sqrt{\frac{kT_e}{2\pi m_e}}\left\{\left(2+\frac{e\Delta\phi_{//}}{kT_e}\right) - \left[\frac{e\Delta\phi_{//}}{kT_e} + 2\left(1-\frac{B_m}{B_i}\right)\right]e^{\frac{e\Delta\phi_{//}}{\left(\frac{B_i}{B_m}-1\right)kT_e}}\right\}, \tag{12}$$

where n_e and T_e are the density and temperature of the magnetospheric electrons originating in the magnetosheath/LLBL and B_i and B_m are the magnetic field intensity in the ionosphere and the magnetosphere, respectively.

[40] The nonlinear equation (10) is discretized using a finite difference method and integrated numerically with a damped Newton iterative scheme and Dirichlet boundary conditions. A set of results is shown in Figures 5 and 6, illustrating $J_{//}$, ε, and Σ_p resulting from a solution of the current continuity equation evaluated at the ionospheric altitude z_i = 200 km. The altitude of the magnetospheric generator is z_m = 90,000 km, that is, the altitude where, in the conical geometry used for mapping, the intensity of the magnetic field is equal to 30 nT, that is, the magnetic field intensity used to derive the kinetic solution describing the magnetosheath/LLBL considered in the model. From the condition that the magnetic flux is conserved and assuming a cylindrical mapping [*Lyons*, 1980], the distance x_m, and the magnetic field B_m at the magnetospheric altitude z_m maps to B_i at the ionospheric altitude z_i, according to the relationship $x_i = x_m\sqrt{B_m/B_i}$. The ionospheric electric potential ϕ_i obtained from equation (10) is introduced back in the analytical expression of $J_{//}$, ε, and Σ_p at the ionospheric altitude z_i. Thus one can obtain these ionospheric electrodynamic parameters associated to the magnetosheath/LLBL generator, as shown in sections 9.2 and 9.3 below.

9.2. Dependencies on Magnetosheath Velocity and Σ_p

[41] Figure 5 shows the model calculation results from three classes of solutions for maximum $J_{//}$, maximum ε, and maximum $\Delta\phi_{//}$ obtained for nonuniform Σ_P with Σ_P = 0.5 S + $\Sigma_P(\varepsilon)$ (solid lines), and Σ_P = 5 S + $\Sigma_P(\varepsilon)$ (dashed lines) as well as for uniform Σ_P = 5 S (dotted lines). The ionospheric feedback introduced by an increase in Σ_P due to higher ε leads to an increase in (1) the maximum $\Delta\phi_{//}$, (2) the maximum ε, and (3) the maximum $J_{//}$.

[42] Given that V_{sw} is positively correlated with magnetosheath V [e.g., *Spreiter and Stahara*, 1985], Figure 5 can be compared with the corresponding quantities derived from DMSP observations plotted in Figure 4. Figure 4 shows that $J_{//}$, maximum peak E_e (proxy for maximum $\Delta\phi_{//}$), and maximum ε all increase with increasing V_{sw}. Figure 5 shows that the maximum $\Delta\phi_{//}$, the maximum ε, and the maximum

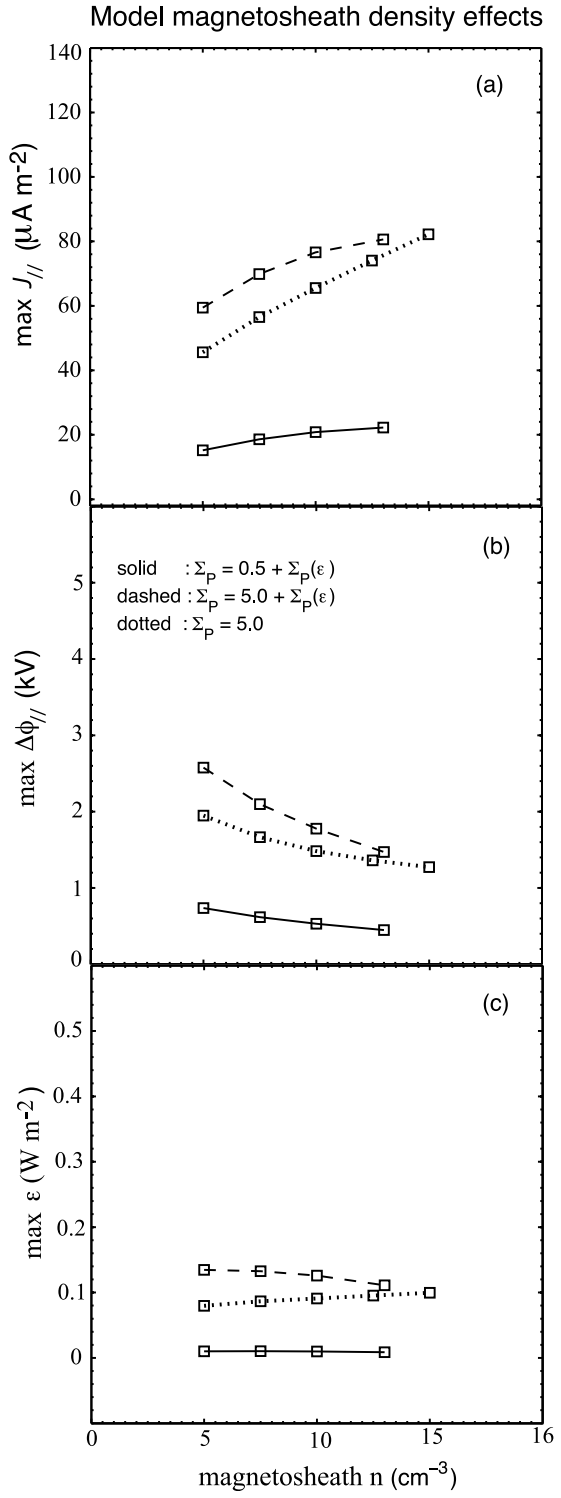

Figure 6. (a) Maximum $J_{//}$, (b) maximum $\Delta\phi_{//}$, and (c) maximum ε as a function of the bulk magnetosheath n and Σ_P. Solid lines represent results obtained for Σ_P that depends on maximum ε with a background conductance $\Sigma_P = 0.5\ S + \Sigma_P(\varepsilon)$, dashed lines show results obtained for a nonuniform conductance with $\Sigma_P = 5\ S + \Sigma_P(\varepsilon)$, and dotted lines correspond to results obtained for a uniform $\Sigma_P = 5$ S. (Adapted from *Echim et al.* [2008].)

$J_{//}$, increase with increasing V at the magnetosheath adjacent to the magnetopause. This is a direct effect of the changes induced in the generator by an increased velocity shear and the quasi-static coupling with the ionosphere. The TD interface generates more electromotive force when the magnetosheath V is higher. This, in turn, leads to the increases in $J_{//}$, maximum $\Delta\phi_{//}$, and maximum ε, as discussed in section 8.

9.3. Dependencies on Magnetosheath Density and Σ_p

[43] Figure 6 summarizes the ionospheric response to changes of n in the inner edge of the magnetosheath. It also shows how these effects depend on the three different models of Σ_p, as was done in section 9.2. Regardless of the conductivities, the maximum $\Delta\phi_{//}$ decreases when magnetosheath n increases and seems to reach a plateau for larger n. The maximum $J_{//}$ increases with magnetosheath n, as shown by Figure 6a. The solution of the current continuity in the topside ionosphere shows strong variations with magnetosheath n due to its role in the current–voltage relationship and the ionospheric feedback described in equations (11) and (12). The variations of $J_{//}$, maximum $\Delta\phi_{//}$, and maximum ε as a function of n in the source region are discussed in section 7.

[44] Given that n_{sw} correlates positively with magnetosheath n [e.g., *Spreiter and Stahara*, 1985], Figure 6 can be compared with the DMSP observations in Figure 3. Figures 3a and 3b show that $J_{//}$ increases with n_{sw} and maximum peak E_e (proxy for maximum $\Delta\phi_{//}$) decreases with increasing n_{sw}, both of which agree qualitatively with the model results plotted in Figures 6a and 6b, respectively. Figure 6c shows that the solution for maximum ε for $\Sigma_p = 0.5\ S + \Sigma_p(\varepsilon)$ does not change much with magnetosheath n. In contrast, the solution for $\Sigma_p = 5\ S + \Sigma_p(\varepsilon)$ slightly decreases with increasing magnetosheath n while the solution for uniform $\Sigma_p = 5$ S increases slightly with increasing magnetosheath n. However, Figure 3c shows that maximum ε does not vary much with respect to n_{sw}. Hence, the trend in the observations agrees best with that for nonuniform conductance with a small base level $\Sigma_p = 0.5\ S + \Sigma_p(\varepsilon)$.

10. $J_{//}$ Dependence on IMF B_z

[45] Up to now, we have examined V_{sw} and n_{sw} effects on $J_{//}$, maximum peak E_e, and maximum ε. IMF B_z has been shown to play a significant role in the SW–magnetosphere interactions. During southward IMF, the reconnection rate is higher and the magnetosphere is more open than during northward IMF. Moreover, the ionospheric convection has been shown to be higher during southward IMF than during northward IMF [*Ruohoniemi and Greenwald*, 1996; *Weimer*, 1995; *Papitashvili et al.*, 1994]. This means that in the flanks, inside the magnetopause, the sunward velocity is higher during southward than northward IMF. Hence, for a given V_{sw}, a higher velocity shear may be expected across the magnetopause boundary for southward IMF than for northward IMF.

[46] Figures 7b and 7f plot $J_{//}$ versus V_{sw} for the afternoon R1 for southward and northward IMF, respectively. As discussed in section 6, near noon the V_{sw} effect and hence the slopes (rates of change) are small because the magnetic field lines access the magnetosheath regions where the

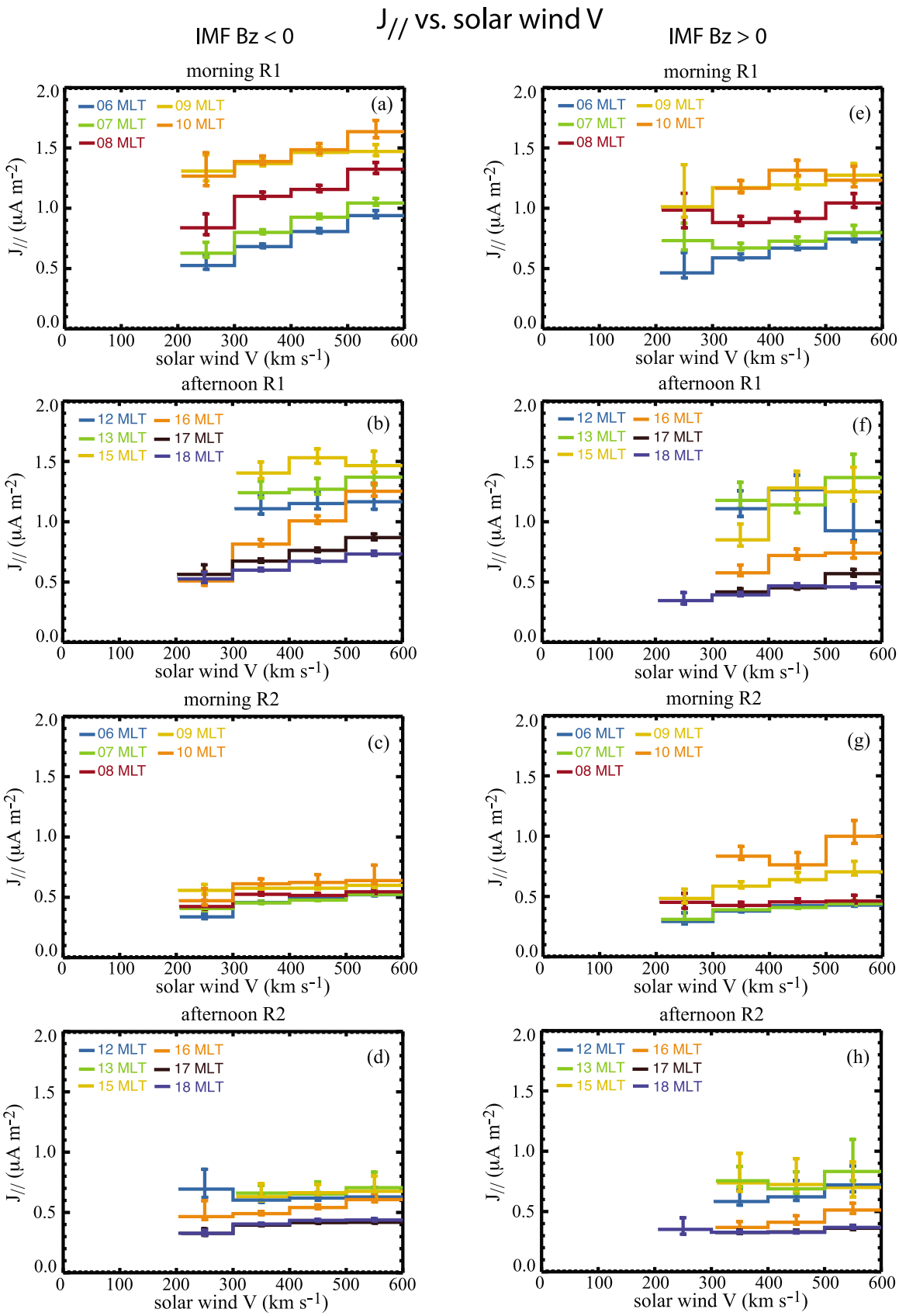

Figure 7. Median $J_{//}$ versus V_{sw} for (a, e) morning R1, (b, f) afternoon R1, (c, g) morning R2, and (d, h) afternoon R2 for IMF $B_z < 0$ (Figures 7a–7d) and for IMF $B_z > 0$ (Figures 7e–7h) in the same format as Figure 2. Median $J_{//}$ values are calculated in 100 km s^{-1} bins.

plasma speed is stagnant or small [e.g., *Spreiter and Stahara*, 1985]. The effect of the higher velocity shear due to higher V_{sw} can be seen in the midafternoon. Figure 7b shows that for southward IMF, the largest slope in the velocity range [200, 600] km s^{-1} is about 1.9 pA s m^{-3} at 16 MLT. In comparison, Figure 7f shows that for northward IMF, the largest slope is almost about half as much, 1.0 pA s m^{-3} at 15 MLT. This would be consistent with the higher velocity shears during southward IMF than during northward IMF.

[47] Figure 7a and 7e plot $J_{//}$ versus V_{sw} for the morning R1 for southward and for northward IMF, respectively. The slopes of the curves at 9–10 MLT are similar for southward and for northward IMF. However, in Figure 7a, for southward IMF, the largest slope found is 1.3 pA s m^{-3} at 8 MLT. In contrast, for northward IMF, in Figure 7e, the slope at 8 MLT is much smaller.

[48] It would be expected that at 6–7 and 17–18 MLT, where the field lines are mostly closed, V_{sw} effect on R1 would vanish, but this is found not to be the case. To be sure, the slopes are smaller near dawn and dusk. This suggests that there may be coupling of V_{sw} with R1 even on closed field lines at these MLTs, albeit the coupling is not as strong as on open-field lines. However, the slopes are higher for southward IMF than for northward IMF, both at dawn and at dusk. For example, at dusk, 18 MLT, the slopes are 0.5 pA s m^{-3} and 0.3 pA s m^{-3} for southward and northward IMF, respectively. At dawn, 6 MLT, the corresponding slopes are 1.0 pA s m^{-3} and 0.63 pA s m^{-3} for southward and northward IMF, respectively.

[49] The slopes are smaller in the $J_{//}$ versus V_{sw} curves for R2 for both morning and afternoon patterns and for northward and southward IMF as can be seen in Figures 7c, 7d, 7g, and 7h. This would be consistent with R2 located on closed field lines as shown in Figure 1. It is interesting and perhaps important to note that although the slopes are smaller, they are not zero. This suggests that there may still be coupling between V_{sw} and R2, even though R2 is located on closed field lines. It is not clear what causes this positive correlation between R2 and V_{sw}. One possibility is that a change in V_{sw} leads to a change in the SW dynamic pressure or merging rate, which, in turn, reconfigures magnetospheric currents, including FACs. This is discussed next in section 11.

11. $J_{//}$ Dependence on SW Dynamic Pressure and Merging Rate

[50] Several studies have shown that an increase/decrease in SW dynamic pressure leads to an increase/decrease in the magnetospheric size and cross-tail, magnetopause, and field-aligned (both R1 and R2) currents in the open and closed regions [e.g., *Rufenach et al.*, 1992; *Wing and Sibeck*, 1997; *Wing et al.*, 2002; *Nakano et al.*, 2009]. *Iijima and Potemra* [1982] report that R1 $J_{//}$ increases with the SW dynamic pressure, but the paper does not show the local time variation of this SW dynamic pressure effect. An increase in SW dynamic pressure can increase the SW–magnetosphere coupling efficiency as manifested in the increased cross-polar cap potential and enhanced ionospheric convection velocities [e.g., *Boudouridis et al.*, 2005; *Siscoe et al.*, 2002]. A change in the ionospheric convection pattern can be linked to changes in FACs in both open and closed field lines from the consideration of the convergence and divergence of horizontal currents and electric field [e.g., *Reiff and Burch*, 1985; *Weimer*, 1999]. Another view of this interaction is that a SW dynamic pressure change launches compressional/rarefactional waves that can mode convert to shear Alfvén waves near the magnetopause or in the magnetosphere that would carry FAC into the ionosphere [e.g., *Kivelson and Southwood*, 1991; *Glassmeier and Heppner*, 1992; *Lysak and Lee*, 1992; *Keller et al.*, 2002].

[51] Merging rates can also affect the SW–magnetospheric coupling efficiency and the cross-polar cap potential [e.g., *Reiff and Luhmann*, 1986], which can affect FACs on open and closed field lines [e.g., *Siscoe and Lu*, 1996; *Russell et al.*, 1994; *Reiff and Burch*, 1985]. A magnetohydrodynamic (MHD) simulation suggests that the merging process generates Alfvén waves that carry FACs to the ionosphere [e.g., *Ma et al.*, 1995].

[52] *Newell et al.* [2007] investigated 20 SW-magnetosphere coupling functions and found that the merging rate correlates best with 10 different indices characterizing the magnetospheric activity. They define merging rate as $d\Phi/dt = V_{sw}^{4/3} B_T^{2/3} \sin^{8/3}(\theta_c/2)$, where B_T = magnetic field line magnitude, and θ_c = arctan (IMF B_y/IMF B_z).

[53] The present study compares how the merging rate and SW dynamic pressure affect R1 and R2 $J_{//}$ at each MLT and how these effects differ from each other. Figures 8a–8d plot $J_{//}$ versus $d\Phi/dt$, while Figures 8e–8h plot $J_{//}$ versus SW dynamic pressure. Note that the X axis range of SW dynamic pressure, 0–5 nPa, covers nearly the full distribution of the SW dynamic pressure [e.g., *Shue et al.*, 1997, Figure 2; *Lee et al.*, 2009, Figure 5]. Similarly, the X axis range of $d\Phi/dt$ in Figure 8 covers nearly the full distribution of $d\Phi/dt$ [e.g., *Newell et al.*, 2007, Figure 3].

[54] Figures 8a and 8b show that $J_{//}$ increases with increasing merging rate, while Figures 8e and 8f show that $J_{//}$ also increases with increasing SW dynamic pressure. However, there are subtle differences between the responses to $d\Phi/dt$ and to SW dynamic pressure. First, the differences between the responses in the open and closed R1 are more noticeable in SW dynamic pressure plots (Figures 8e and 8f) than in $d\Phi/dt$ plots (Figures 8a and 8b). For example, in Figure 8e, the slope at 7 MLT (closed morning R1) is about 0.04 μA (nPa^{-1} m^{-2}) whereas the slope at 10 MLT (open morning R1) is about 0.1 μA (nPa^{-1} m^{-2}). In contrast, in Figure 8a, the slopes for closed morning R1 are similar to those for open morning R1. A similar relationship can be discerned from the afternoon R1 shown in Figures 8b and 8f. In Figure 8f, the slopes of 17 and 18 MLT curves are smaller than those of 13, 15, and 16 MLT curves. In contrast, the differences are smaller among the curves at 13, 15, 17, and 18 MLT in Figure 8b.

[55] Second, the responses to $d\Phi/dt$ appear to be noticeably stronger than those to SW dynamic pressure in the closed R1, at 6–8 and 16–18 MLT. This can be seen in Figures 8a, 8b, 8e, and 8f. Similarly, the slopes of the R2 $J_{//}$ versus $d\Phi/dt$ curves appear to be larger than those of $J_{//}$ versus SW dynamic pressure in most MLTs.

[56] From Figures 2a and 2b, it can be discerned that closed R1 $J_{//}$ does not change much with n_{sw}. Thus, closed R1 $J_{//}$ response to SW dynamic pressure is almost entirely due to the V_{sw} term. Note that the merging rate does not have the n_{sw} term.

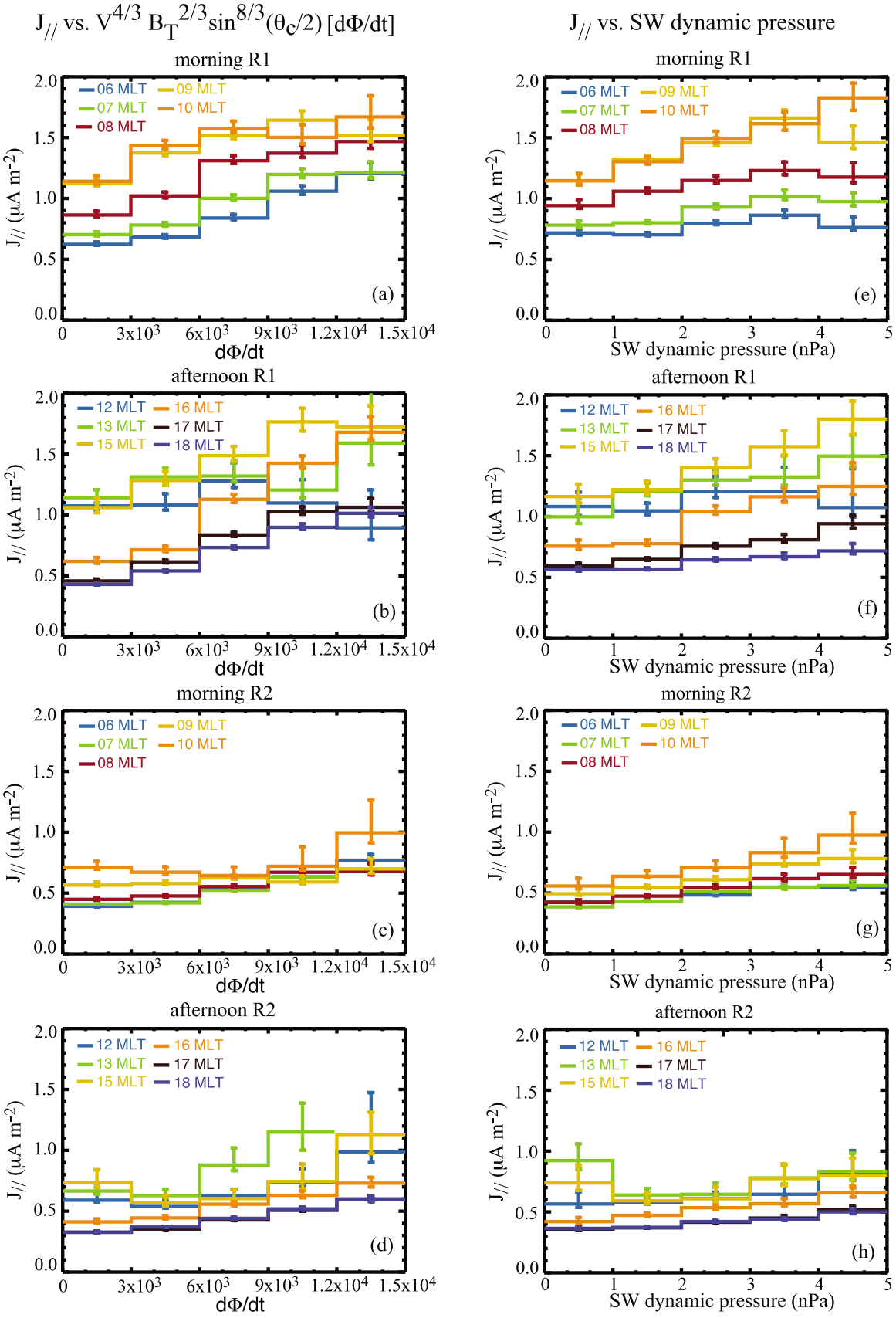

Figure 8. (a–d) Median $J_{//}$ as a function of merging rate ($d\Phi/dt = V_{sw}^{4/3} B_T^{2/3} \sin^{8/3}(\theta_c/2)$) and (e–h) SW dynamic pressure in the same format as Figure 2.

[57] Figure 8 shows that the effects of $d\Phi/dt$ and SW dynamic pressure are more modest on R2 than R1 regardless of the MLT. This is consistent with the view that R1 is more open than R2. The weak responses of R2 to SW dynamic pressure, especially near dusk and dawn, are consistent with the finding for nonstorm times by *Nakano et al.* [2009], although here we show that there is an MLT variation.

12. Summary and Conclusion

[58] Solar wind provides the electromagnetic force that drives FAC at the magnetopause boundary layer. The velocity shear between the antisunward magnetosheath plasma flow and the adjacent nearly stagnant magnetospheric plasma generates a voltage drop across the magnetopause. The coupling of this voltage drop with the ionosphere through the magnetic field creates a complex electric circuit linking $J_{//}$, $\Delta\phi_{//}$, ε, ionospheric conductivity, ionospheric currents, and ionospheric cross-polar cap potential drop.

[59] The present study investigates how simultaneously or nearly simultaneously observed SW and IMF affect dayside $J_{//}$, $\Delta\phi_{//}$, and ε with DMSP observations and the *Echim et al.* [2007, 2008] model. Our findings are summarized below.

[60] 1. The open and closed nature of R1 and R2 inferred from the simultaneous SW and DMSP magnetometer observations is consistent with that obtained from simultaneous DMSP SSJ4 and DMSP magnetometer observations obtained by *Wing et al.* [2010], as shown in Figure 1.

[61] 2. In general, R1 $J_{//}$ dependency on n_{sw} is largest near noon and gradually decreases toward dawn and dusk. This can be attributed to the magnetosheath n evolution along the magnetopause. At the subsolar stagnation point, magnetosheath n is highest near noon and gradually decreases away toward the nightside as the magnetosheath flow increases antisunwardly.

[62] 3. R1 $J_{//}$ has also a dependency on V_{sw}, but unlike n_{sw}, the largest dependency is in the midafternoon, 15–16 MLT and in the midmorning, 8 MLT. This can also be attributed to the magnetosheath evolution along the magnetopause. The magnetosheath flow nearly stagnates at the subsolar points and gradually increases toward the nightside. At 17–18 MLT and 6–7 MLT, the field lines become more frequently closed and R1 $J_{//}$ dependency on V_{sw} is weaker.

[63] 4. Within R2, near dusk R1, and near dawn R1, $J_{//}$ exhibits only weak dependencies on n_{sw} and V_{sw} because these FACs are located mostly on closed field lines.

[64] 5. In the open R1 at 12–16 MLT, an increase in n_{sw} increases K and $J_{//}$, but decreases the maximum peak E_e (or $\Delta\phi_{//}$), in accordance with the linearized Knight relation [*Knight*, 1973] and the expressions in equations (1)–(8), provided that other parameters are held constant. Maximum ε appears insensitive to n_{sw} because peak E_e varies inversely with n_{sw} and the effects of the two terms nearly cancel each other.

[65] 6. In the open R1 at 12–16 MLT, an increase in V_{sw} increases $J_{//}$, maximum peak E_e (or $\Delta\phi_{//}$), and maximum ε due to an increase of the velocity shear at the magnetopause boundary, which leads to higher electric potential drop across the boundary.

[66] 7. It is appropriate to discuss the 12–16 MLT R1 $J_{//}$ responses to n_{sw} and V_{sw} using the linearized Knight relation [*Knight*, 1973; *Lyons et al.*, 1979] because the currents flow upward and SW electrons provide the current carriers. Interestingly, morning R1 at 9–10 MLT, which flows downward, exhibits the same responses.

[67] 8. In the open region, the response of $J_{//}$ to V_{sw} is higher for southward than for northward IMF. This can be attributed to the higher velocity shear at the magnetopause due to the higher sunward convection within the magnetosphere for southward IMF [e.g., *Ruohoniemi and Greenwald*, 1996; *Weimer*, 1995; *Papitashvili et al.*, 1994].

[68] 9. Both R1 and R2 $J_{//}$ increase with increasing SW dynamic pressure and merging rate, but the biggest differences between the two effects can be found in the closed R1 near dawn and dusk. At these local times, R1 $J_{//}$ is more sensitive to merging rate than to SW dynamic pressure.

[69] **Acknowledgments.** The study was supported by NSF Grants ATM-0703445, ATM-0802715, and ATM-0538513, and by NASA Grant NNX10AE63G. Shin Ohtani acknowledges the support of NSF grant ATM-0503065 and NASA Grant NNX09AF46G. Marius Echim acknowledges support from the Belgian Office for Science (BELSPO) grant MO/35/031 and from ESA PECS grant 98049/2007. Jay R. Johnson acknowledges support from NASA grants (NNG07EK69I, NNH07AF37I, NNH09AM53I, and NNH09AK63I), NSF grant ATM0902730, and DOE contract DE-AC02-09CH11466. We thank Fred Rich and the Air Force Research Laboratory for the DMSP SSJ4 and magnetometer data. We thank James M. Weygand for the solar wind data processing. The raw solar wind data from ACE, Wind, IMP8, ISEE1 and ISEE3 were obtained from NASA CDAW and NSSDC.

[70] Masaki Fujimoto thanks the reviewers for their assistance in evaluating this manuscript.

References

Anderson, B. J., H. Korth, C. L. Waters, D. L. Green, and P. Stauning (2008), Statistical Birkeland current distributions from magnetic field observations by the Iridium constellation, *Ann. Geophys.*, *26*, 671–687, doi:10.5194/angeo-26-671-2008.

Axford, W. I., and C. O. Hines (1974), A unifying theory of high-latitude geophysical phenomena and geomagnetic storms, in *The Upper Atmosphere in Motion*, edited by C. O. Hines et al., pp. 933–967, AGU, Washington D. C.

Bame, S. J., D. J. McComas, B. L. Barraclough, J. L. Phillips, K. J. Sofaly, J. C. Chavez, B. E. Glostein, and R. K. Sakurai (1992), The Ulysses solar wind plasma experiment, *Astron. Astrophys. Suppl. Ser.*, *92*, 237–265.

Borovsky, J. E., M. F. Thomsen, and R. C. Elphic (1998), The driving of the plasma sheet by the solar wind, *J. Geophys. Res.*, *103*, 17,617–17,639, doi:10.1029/97JA02986.

Boudouridis, A., E. Zesta, L. R. Lyons, P. C. Anderson, and D. Lummerzheim (2005), Enhanced solar wind geoeffectiveness after a sudden increase in dynamic pressure during southward IMF orientation, *J. Geophys. Res.*, *110*, A05214, doi:10.1029/2004JA010704.

Burch, J. L., P. H. Reiff, and M. Sugiura (1983), Upward electron beams measured by DE-1: A primary source of dayside region-1 Birkeland currents, *Geophys. Res. Lett.*, *10*, 753–756, doi:10.1029/GL010i008p00753.

Chiu, Y. T., and M. Schultz (1978), Self-consistent particle and parallel electrostatic field distribution in the magnetospheric-ionospheric auroral region, *J. Geophys. Res.*, *83*, 629–642, doi:10.1029/JA083iA02p00629.

De Keyser, J., M. Roth, and J. Lemaire (1998), The magnetospheric driver of subauroral ion drifts, *Geophys. Res. Lett.*, *25*, 1625–1628, doi:10.1029/98GL01135.

Dungey, J. W. (1961), Interplanetary magnetic field and the auroral zone, *Phys. Rev. Lett.*, *6*, 47, doi:10.1103/PhysRevLett.6.47.

Eastman, T. E., E. W. Hones Jr., S. J. Bame, and J. R. Asbridge (1976), The magnetospheric boundary layer: Site of plasma, momentum, and energy transfer from the magnetosheath into the magnetosphere, *Geophys. Res. Lett.*, *3*, 685–688, doi:10.1029/GL003i011p00685.

Echim, M., and J. Lemaire (2005), Two-dimensional Vlasov solution for a collisionless plasma jet across transverse magnetic field lines with a sheared bulk velocity, *Phys. Rev. E*, *72*, 036405, doi:10.1103/PhysRevE.72.036405.

Echim, M. M., M. Roth, and J. De Keyser (2007), Shared magnetospheric plasma flows and discrete auroral arcs: A quasi-static coupling model, *Ann. Geophys.*, *25*, 317–330, doi:10.5194/angeo-25-317-2007.

Echim, M. M., M. Roth, and J. De Keyser (2008), Ionospheric feedback effects on the quasi-static coupling between LLBL and postnoon/evening discrete auroral arcs, *Ann. Geophys.*, *26*, 913–928, doi:10.5194/angeo-26-913-2008.

Echim, M. M., R. Maggiolo, M. Roth, and J. De Keyser (2009), A magnetospheric generator driving ion and electron acceleration and electric currents in a discrete auroral arc observed by Cluster and DMSP, *Geophys. Res. Lett.*, *36*, L12111, doi:10.1029/2009GL038343.

Fridman, M., and J. Lemaire (1980), Relationship between auroral electron fluxes and field-aligned electric potential differences, *J. Geophys. Res.*, *85*, 664–670, doi:10.1029/JA085iA02p00664.

Glassmeier, K.-H., and C. Heppner (1992), Traveling magnetospheric convection twin-vortices: Another case study, global characteristics, and a model, *J. Geophys. Res.*, *97*, 3977, doi:10.1029/91JA02464.

Hardy, D. A., L. K. Schmitt, M. S. Gussenhoven, F. J. Marshall, H. C. Yeh, T. L. Shumaker, A. Hube, and J. Pantazis (1984), Precipitating electron and ion detectors (SSJ/4) for the block 5D/flights 6–10 DMSP satellites: Calibration and data presentation, *Rep. AFGL-TR-84-0317*, Air Force Geophys. Lab., Hanscom Air Force Base, Mass.

Harel, M., R. Wolf, P. Reiff, and H. Hillis (1977), Study of plasma flow near the Earth's plasma pause, *Tech. Rep. AFGL-TR-77-286*, U.S. Air Force Geophys. Lab., Hanscom Air Force Base, Mass.

Hasegawa, H., M. Fujimoto, K. Maezawa, Y. Saito, and T. Mukai (2003), Geotail observations of the dayside outer boundary region: Interplanetary magnetic field control and dawn-dusk asymmetry, *J. Geophys. Res.*, *108*(A4), 1163, doi:10.1029/2002JA009667.

Higuchi, T., and S. Ohtani (2000), Automatic identification of large-scale field-aligned current structures, *J. Geophys. Res.*, *105*, 25,305, doi:10.1029/2000JA900073.

Hodges, J. L., Jr., and E. L. Lehmann (1967), On medians and quasi medians, *J. Am. Stat. Assoc.*, *62*(319), 926–931, doi:10.2307/2283680.

Iijima, T., and T. A. Potemra (1982), The relationship between interplanetary quantities and Birkeland current densities, *Geophys. Res. Lett.*, *9*, 442–445, doi:10.1029/GL009i004p00442.

Johnson, J. R., and S. Wing (2009), Northward internplanetary magnetic field plasma sheet entropies, *J. Geophys. Res.*, *114*, A00D08, doi:10.1029/2008JA014017.

Keller, K. A., M. Hesse, M. Kuznetsova, L. Rastatter, T. Moretto, T. I. Gombosi, and D. L. DeZeeuw (2002), Global MHD modeling of the impact of a solar wind pressure change, *J. Geophys. Res.*, *107*(A7), 1126, doi:10.1029/2001JA000060.

Kenney, J. F., and E. S. Keeping (1951), *Mathematics of Statistics Part Two*, 2nd ed., Van Nostrand Reinhold, Princeton, N. J.

Kivelson, M., and D. Southwood (1991), Ionospheric traveling vortex generation by solar wind buffeting of the magnetosphere, *J. Geophys. Res.*, *96*, 1661, doi:10.1029/90JA01805.

Knight, L. (1973), Parallel electric fields, *Planet. Space Sci.*, *21*, 741–750, doi:10.1016/0032-0633(73)90093-7.

Lee, C. O., J. G. Luhmann, D. Odstrcil, P. J. MacNeice, I. de Pater, P. Riley, and C. N. Arge (2009), The solar wind at 1 AU during the declining phase of solar cycle 23: Comparison of 3D numerical model results with observations, *Sol. Phys.*, *254*, 155–183, doi:10.1007/s11207-008-9280-y.

Lemaire, J., and M. Scherer (1973), Plasma sheet particle precipitation: A kinetic model, *Planet. Space Sci.*, *21*, 281–289, doi:10.1016/0032-0633(73)90012-3.

Lockwood, M., P. E. Sandholt, S. W. H. Cowley, and T. Oguti (1989), Interplanetary magnetic field control of dayside auroral activity and transfer of momentum across the dayside magnetopause, *Planet. Space Sci.*, *37*, 1347–1365, doi:10.1016/0032-0633(89)90106-2.

Lyons, L. R. (1980), Generation of large-scale regions of auroral currents, electric potentials and precipitation by the divergence of the convection electric field, *J. Geophys. Res.*, *85*, 17–24, doi:10.1029/JA085iA01p00017.

Lyons, L. R. (1981), Discrete aurora as the direct result of an inferred high altitude generating potential distribution, *J. Geophys. Res.*, *86*, 1–8, doi:10.1029/JA086iA01p00001.

Lyons, L. R., D. S. Evans, and R. Lundin (1979), An observed relation between magnetic field aligned electric fields and downward electron energy fluxes in the vicinity of auroral forms, *J. Geophys. Res.*, *84*, 457–461, doi:10.1029/JA084iA02p00457.

Lysak, R. L., and D.-H. Lee (1992), Response of the dipole magnetosphere to pressure pulses, *Geophys. Res. Lett.*, *19*, 937, doi:10.1029/92GL00625.

Ma, Z. W., L. C. Lee, and A. Otto (1995), Generation of field-aligned currents and Alfvén waves by 3D magnetic reconnection, *Geophys. Res. Lett.*, *22*, 1737–1740, doi:10.1029/95GL01430.

Nakano, S., G. Ueno, S. Ohtani, and T. Higuchi (2009), Impact of the solar wind dynamic pressure on the Region 2 field-aligned currents, *J. Geophys. Res.*, *114*, A02221, doi:10.1029/2008JA013674.

Newell, P. T., and C.-I. Meng (1988), The cusp and the cleft/boundary layer: Low-altitude identification and statistical local time variation, *J. Geophys. Res.*, *93*, 14,549–14,556, doi:10.1029/JA093iA12p14549.

Newell, P. T., and C.-I. Meng (1992), Mapping the dayside ionosphere to the magnetosphere according to particle precipitation characteristics, *Geophys. Res. Lett.*, *19*, 609–612, doi:10.1029/92GL00404.

Newell, P. T., and C.-I. Meng (1994), Ionospheric projections of magnetospheric regions under low and high solar wind dynamic pressure, *J. Geophys. Res.*, *99*, 273–286, doi:10.1029/93JA02273.

Newell, P. T., W. J. Burke, C.-I. Meng, E. R. Sanchez, and M. E. Greenspan (1991a), Identification and observations of the plasma mantle at low altitude, *J. Geophys. Res.*, *96*, 35–45, doi:10.1029/90JA01760.

Newell, P. T., S. Wing, C. I. Meng, and V. Sigillito (1991b), The auroral oval position, structure and intensity of precipitation from 1984 onwards: An automated on-line data base, *J. Geophys. Res.*, *96*, 5877–5882, doi:10.1029/90JA02450.

Newell, P. T., W. J. Burke, E. R. Sanchez, C.-I. Meng, M. E. Greenspan, and C. R. Clauer (1991c), The low-latitude boundary layer and the boundary plasma sheet at low altitude: Prenoon precipitation regions and convection reversal boundaries, *J. Geophys. Res.*, *96*, 21,013–21,023, doi:10.1029/91JA01818.

Newell, P. T., J. M. Ruohoniemi, and C.-I. Meng (2004), Maps of precipitation by source region, binned by IMF, with inertial convection streamlines, *J. Geophys. Res.*, *109*, A10206, doi:10.1029/2004JA010499.

Newell, P. T., T. Sotirelis, K. Liou, C.-I. Meng, and F. J. Rich (2007), A nearly universal solar wind-magnetosphere coupling function inferred from 10 magnetospheric state variables, *J. Geophys. Res.*, *112*, A01206, doi:10.1029/2006JA012015.

Ohtani, S., and T. Higuchi (2000), Four-sheet structures of dayside field-aligned currents: Statistical study, *J. Geophys. Res.*, *105*, 25,317–25,324, doi:10.1029/2000JA900074.

Papitashvili, V. O., B. A. Belov, D. S. Faermark, Y. I. Feldstein, S. A. Golyshev, L. I. Gromova, and A. E. Levitin (1994), Electric potential patterns n the northern and southern polar regions parameterized by the interplanetary magnetic field, *J. Geophys. Res.*, *99*, 13,251–13,262, doi:10.1029/94JA00822.

Papitashvili, V. O., R. Christiansen, and T. Neubert (2002), A new model of field-aligned currents derived from high-precision satellite magnetic field data, *Geophys. Res. Lett.*, *29*(14), 1683, doi:10.1029/2001GL014207.

Pierrard, V. (1996), New model of magnetospheric current-voltage relationship, *J. Geophys. Res.*, *101*, 2669–2675, doi:10.1029/95JA00476.

Reiff, P. H., and J. L. Burch (1985), IMF B_y-dependent plasma flow and Birkeland currents in the dayside magnetosphere: 2. A global mode for northward and southward IMF, *J. Geophys. Res.*, *90*, 1595–1609, doi:10.1029/JA090iA02p01595.

Reiff, P. H., and J. G. Luhmann (1986), Solar wind control of the polar-cap voltage, in *Solar Wind-Magnetosphere Coupling*, edited by Y. Kamide and J. A. Slavin, pp. 453–476, Terra Sci., Tokyo.

Reiff, P. H., H. L. Collin, J. D. Craven, J. L. Burch, J. D. Winningham, E. G. Shelley, L. A. Frank, and M. A. Friedman (1988), Determination of auroral electrostatic potentials using high- and low-altitude particle distributions, *J. Geophys. Res.*, *93*, 7441–7465, doi:10.1029/JA093iA07p07441.

Rich, F. J., D. A. Hardy, and M. S. Gussenhoven (1985), Enhanced ionosphere-magnetosphere data from the DMSP satellites, *Eos*, *66*, 513.

Robinson, R. M., and R. R. Vondrak (1984), Measurements of E region ionization and conductivity produced by solar illumination at high latitudes, *J. Geophys. Res.*, *89*, 3951–3956, doi:10.1029/JA089iA06p03951.

Rostoker, G., M. Mareschal, and J. C. Samson (1982), Response of dayside net downward field-aligned current to changes in the interplanetary magnetic field and to substorm perturbations, *J. Geophys. Res.*, *87*, 3489–3510, doi:10.1029/JA087iA05p03489.

Roth, M., J. de Keyser, and M. Kuznetsova (1996), Vlasov theory of the equilibrium structure of tangential discontinuities in space plasmas, *Space Sci. Rev.*, *76*, 251–317, doi:10.1007/BF00197842.

Rufenach, C. L., R. L. McPherron, and J. Schaper (1992), The quiet geomagnetic field at geosynchronous orbit and its dependence on solar wind dynamic pressure, *J. Geophys. Res.*, *97*, 25–42, doi:10.1029/91JA02135.

Ruohoniemi, J. M., and R. A. Greenwald (1996), Statistical patterns of high-latitude convection obtained from Goose Bay HF radar observations, *J. Geophys. Res.*, *101*, 21,743–21,763, doi:10.1029/96JA01584.

Russell, C. T., M. Ginskey, and S. M. Petrinec (1994), Sudden impulses at low latitude stations: Steady state response for southward interplanetary magnetic field, *J. Geophys. Res.*, *99*, 13,403–13,408, doi:10.1029/94JA00549.

Samsonov, A. A., and D. Hubert (2004), Steady state slow shock inside the Earth's magnetosheath: To be or not to be? 2. Numerical three-

dimensional MHD modeling, *J. Geophys. Res.*, *109*, A01218, doi:10.1029/2003JA010006.
Shue, J.-H., J. K. Chao, H. C. Fu, C. T. Russell, P. Song, K. K. Khurana, and H. J. Singer (1997), A new functional form to study the solar wind control of the magnetopause size and shape, *J. Geophys. Res.*, *102*, 9497–9511, doi:10.1029/97JA00196.
Siscoe, G., and G. Lu (1996), Dayside Birkeland currents during substorms: An AMIE test of a substorm model, *J. Geophys. Res.*, *101*, 19,937–19,940, doi:10.1029/96JA01874.
Siscoe, G. L., W. Lotko, and B. U. O. Sonnerup (1991), A high-latitude, low-latitude boundary layer model of convection current system, *J. Geophys. Res.*, *96*, 3487–3495, doi:10.1029/90JA02362.
Siscoe, G. L., G. M. Erickson, B. U. Ö. Sonnerup, N. C. Maynard, J. A. Schoendorf, K. D. Siebert, D. R. Weimer, W. W. White, and G. R. Wilson (2002), Hill model of transpolar potential saturation: Comparisons with MHD simulations, *J. Geophys. Res.*, *107*(A6), 1075, doi:10.1029/2001JA000109.
Sonnerup, B. U. Ö. (1980), Theory of the low-latitude boundary layer, *J. Geophys. Res.*, *85*, 2017–2026, doi:10.1029/JA085iA05p02017.
Spreiter, J. R., and S. S. Stahara (1985), Magnetohydrodynamic and gasdynamic theories for planetary bow waves, in *Collisionless Shocks in the Heliosphere: Reviews of Current Research*, *Geophys. Monogr. Ser*, vol. 35, edited by B. T. Tsurutani and R. G. Stone, pp. 85–107, AGU, Washington, D. C.
Stern, D. P. (1983), The origins of Birkeland currents, *Rev. Geophys. Space Phys.*, *21*, 125–138, doi:10.1029/RG021i001p00125.
Taguchi, S., M. Sugiura, J. D. Winnigham, and J. A. Slavin (1993), Characterization of the IMF By-dependent field-aligned currents in the cleft region based on DE 2 observations, *J. Geophys. Res.*, *98*, 1393–1407, doi:10.1029/92JA01014.
Vennerstrom, S., T. Moretto, L. Rastätter, and J. Raeder (2005), Field-aligned currents during northward interplanetary magnetic field: Morphology and causes, *J. Geophys. Res.*, *110*, A06205, doi:10.1029/2004JA010802.
Weimer, D. R. (1995), Models of high-latitude electric potentials derived with a least error fit of spherical harmonic coefficients, *J. Geophys. Res.*, *100*, 19,595–19,607, doi:10.1029/95JA01755.
Weimer, D. R. (1999), Substorm influence on the ionospheric electric potentials and currents, *J. Geophys. Res.*, *104*, 185–197, doi:10.1029/1998JA900075.
Weimer, D. R. (2001), Maps of ionospheric field-aligned currents as a function of the interplanetary magnetic field derived from Dynamics Explorer 2 data, *J. Geophys. Res.*, *106*, 12,889–12,902, doi:10.1029/2000JA000295.
Weimer, D. R., D. M. Ober, N. C. Maynard, M. R. Collier, D. J. McComas, N. F. Ness, C. W. Smith, and J. Watermann (2003), Predicting interplanetary magnetic field (IMF) propagation delay times using the minimum variance technique, *J. Geophys. Res.*, *108*(A1), 1026, doi:10.1029/2002JA009405. [Correction, *J. Geophys. Res.*, *109*, A12104, doi:10.1029/2004JA010691, 2004.]
Wing, S., and P. T. Newell (2000), Quiet time plasma sheet ion pressure contribution to Birkeland currents, *J. Geophys. Res.*, *105*, 7793–7802, doi:10.1029/1999JA900464.
Wing, S., and D. G. Sibeck (1997), The effects of interplanetary magnetic field Z-component and the solar wind dynamic pressure on the magnetospheric magnetic field line, *J. Geophys. Res.*, *102*, 7207–7216, doi:10.1029/97JA00150.
Wing, S., P. T. Newell, and T. G. Onsager (1996), Modeling the Entry of the Magnetosheath Electrons into the Dayside Ionosphere, *J. Geophys. Res.*, *101*, 13,155–13,167, doi:10.1029/96JA00395.
Wing, S., P. T. Newell, and J. M. Ruohoniemi (2001), Double cusp: Model prediction and observational verification, *J. Geophys. Res.*, *106*, 25,571–25,593, doi:10.1029/2000JA000402.
Wing, S., D. G. Sibeck, M. Wiltberger, and H. Singer (2002), Geosynchronous magnetic field temporal response to the solar wind and IMF variations, *J. Geophys. Res.*, *107*(A8), 1222, doi:10.1029/2001JA009156.
Wing, S., J. R. Johnson, P. T. Newell, and C.-I. Meng (2005), Dawn-dusk asymmetry in the northward IMF plasma sheet, *J. Geophys. Res.*, *110*, A08205, doi:10.1029/2005JA011086.
Wing, S., J. R. Johnson, and M. Fujimoto (2006), Timescale for the formation of the cold-dense plasma sheet: A case study, *Geophys. Res. Lett.*, *33*, L23106, doi:10.1029/2006GL027110.
Wing, S., S. Ohtani, P. T. Newell, T. Higuchi, G. Ueno, and J. M. Weygand (2010), Dayside field-aligned current source regions, *J. Geophys. Res.*, *115*, A12215, doi:10.1029/2010JA015837.
Zaharia, S., and C. Z. Cheng (2003), Near-Earth thin current sheets and Birkeland currents during substorm growth phase, *Geophys. Res. Lett.*, *30*(17), 1883, doi:10.1029/2003GL017456.

M. Echim, Institut d'Aeronomie Spatiale de Belgique, Ringlaan 3, Brussels B-1180, Belgium.
T. Higuchi and G. Ueno, Department of Statistical Modeling, Institute of Statistical Mathematics, 4-6-7 Minami-Azabu, Minato-ku, Tokyo 106-8569, Japan.
J. R. Johnson, Plasma Physics Laboratory, Princeton University, Rt. 1 N, MS 28, Princeton, NJ 08543, USA.
S. Ohtani, P. T. Newell, and S. Wing, Johns Hopkins University Applied Physics Laboratory, 11100 Johns Hopkins Rd., Laurel, MD 20723, USA. (simon.wing@jhuapl.edu)
G. R. Wilson, Air Force Research Laboratory, 11708 San Victorio Ave. NE, Albuquerque, NM 87111, USA.